

# Deep Spatio-temporal Sparse Decomposition for Trend Prediction and Anomaly Detection in Cardiac Electrical Conduction

Xinyu Zhao<sup>1</sup>, Hao Yan<sup>1</sup>, Zhiyong Hu<sup>2</sup>, Dongping Du<sup>2 \*†‡</sup>

## Abstract

Electrical conduction among cardiac tissue is commonly modeled with partial differential equations, i.e., reaction-diffusion equation, where the reaction term describes cellular stimulation and diffusion term describes electrical propagation. Detecting and identifying of cardiac cells that produce abnormal electrical impulses in such nonlinear dynamic systems are important for efficient treatment and planning. To model the nonlinear dynamics, simulation has been widely used in both cardiac research and clinical study to investigate cardiac disease mechanisms and develop new treatment designs. However, existing cardiac models have a great level of complexity, and the simulation is often time-consuming. We propose a deep spatio-temporal sparse decomposition (DSTSD) approach to bypass the time-consuming cardiac partial differential equations with the deep spatio-temporal model and detect the time and location of the anomaly (i.e., malfunctioning cardiac cells). This approach is validated from the data set generated from the Courtemanche-Ramirez-Nattel (CRN) model, which is widely used to model the propagation of the transmembrane potential across the cross neuron membrane. The proposed DSTSD achieved the best accuracy in terms of spatio-temporal mean trend prediction and anomaly detection.

## 1 Introduction

Cardiac arrhythmia is a group of conditions where the heartbeat is irregular. Common conditions include ventricular tachycardia, atrial flutter, ventricular fibrillation, etc. These conditions occur when abnormal and chaotic electrical impulses cause heart chambers to quiver ineffectively instead of pumping blood to support the body. Such abnormal activities can result in serious complications such as stroke and even

---

\*This work was supported in part by National Science Foundation under Grant DMS-1830363, CMMI-1646664, CMMI 1922739, and CMMI-1728338.

<sup>†</sup>Xinyu Zhao and Hao Yan <sup>1</sup> are with School of Computing, Informatics, and Decision Systems Engineering, Arizona State University, Tempe, AZ 85281, USA. (e-mail: haoyan@asu.edu).

<sup>‡</sup>Zhiyong Hu and Dongping Du <sup>2</sup> are with Industrial, Manufacturing & Systems Engineering in Texas Tech University, Lubbock, TX 79409, USA (email: Dongping.Du@ttu.edu)

sudden death. For arrhythmias that can not be treated with medications, surgical procedures can be done to locate abnormal cardiac cells that initiate disorders and burn the tissue to stop the abnormal electrical activities. However, the identification of abnormal electrical impulses and problematic tissue is challenging.

Detection and identification of the cardiac cells that cause arrhythmia can be defined as an anomaly detection problem. Anomaly detection is not a new concept in cardiac research. Many studies have been done to identify dissimilar heartbeats in Electrocardiogram (ECG) to aid cardiac diagnosis. The majority of these studies use signal processing and machine learning techniques to distinguish unusual waveforms in ECG and detect abnormal cardiac events [1]. In addition, works have been done to detect anomalies in time series of multi-parameter clinical data to distinguish critical from non-critical conditions for patients undergoing heart surgery [2]. Most of the existing studies focus on analyzing raw time series data to detect abnormal patterns. Currently, the identification of cardiac cells that initiate and maintain irregular electrical activities remains challenging. This paper focuses on detecting and locating dissimilar cellular stimulation (i.e., *anomaly*) from a large number of *normal* cells whose transmembrane potentials either stay at a constant value or vary regularly in a normal way by analyzing signals (i.e., changes of transmembrane potential overtime) generated from individual cells. Detecting when and which cells initiate the abnormal electrical impulses is important for efficient treatment design and planning. More literature on anomaly detection based on the cardiac electrical conduction will be discussed in Section 2.1.

There are significant challenges involved in detecting the anomaly from normal cardiac electrical activities. The first challenge is that normal cardiac activities usually present very *complicated spatio-temporal patterns*. To study such patterns, computer models across different organizational scales, including cellular models, tissue models, and organ models, are often used. The cardiac cell model describes the transmembrane potential as a function of time by an ordinary differential equation, and the measurement of the transmembrane potential waveform signifying the electrical activity of cardiac cells is known as action potential [3]. The propagation of electrical waves in cardiac tissue is modeled by a reaction-diffusion equation where the reaction term describes the cellular stimulation, and the diffusion term represents cell-to-cell interactions. For example, the Courtemanche-Ramirez-Nattel (CRN) model was developed [4], which consists of over seventy coupled equations to describe cardiac depolarization and repolarization.

The second challenge is that anomaly can happen at any location, time, and magnitude with complex spatio-temporal propagation behavior. This paper aims to model the premature firing of the transmembrane potentials due to either abnormal diastolic depolarization or after repolarization, which is one of the major causes of cardiac arrhythmia, such as atrial fibrillation. In the experiments, the regular/periodic stimulation triggers the normal electrical conduction, and the irregular/random stimulation is given to trigger abnormal stimulation. We are interested in detecting abnormal stimulation from regular and periodic electrical activ-

ities. Anomaly, due to the remodeling of individual cardiac cells, is often sparse. One specific challenge is that if the anomaly is not detected timely after its initiation, it will be propagated throughout the entire system and become hard to identify the exact time and location when or where it starts.

The third challenge is that although many simulation models such as CRN provides accurate quantification of cardiac cellular functions, they may suffer from high computational time and unknown parameters. For example, when the cardiac model extends to the higher organizational scales, e.g., tissue and organ scales, the simulation is very time-demanding. Furthermore, the identification and customization of the CRN model to specific applications are challenging since it involves unobservable variables (e.g., ion channel gating variables), which are difficult to measure in in-vitro/in-vivo experiments.

To address these challenges, we propose to learn a metamodel to replace the time-consuming simulation models. Cardiac electrical propagation is inherently a spatio-temporal process with transmembrane potential changing in a nonlinear fashion in the temporal domain and electrical waves propagating in the spatial domain. Therefore, deep spatio-temporal models can be constructed to learn the hidden dynamics in the spatio-temporal processes. Deep neural networks such as convolutional neural networks [5] and recurrent neural networks [6] have been proved as efficient models to describe the complex spatio-temporal processes. For example, deep learning has recently been used as a metamodel to replace the traditional partial differential equations (PDE) in cardiac simulation and has achieved great prediction accuracy [7]. This can be realized by learning the hidden dynamics of the spatio-temporal process from simulation data generated by realistic cardiac models.

In many cases, it is important not only to model the normal spatio-temporal patterns but also to detect when and where the anomaly would happen (i.e., the cardiac cells that produce irregular electrical impulses). In literature, spatial-temporal smooth-sparse decomposition was proposed to detect sparse anomalies from the smooth spatial and temporal mean trend [8]. However, due to the assumption of the linear basis representation for the complicated spatio-temporal foreground, it is not suitable to model complicated spatio-temporal patterns in the cardiac electrical conduction. Furthermore, since the time interval of such impulse is short and the anomaly pattern follows the same spatiotemporal propagation rule (e.g., CRN equation) according to the normal patterns. Therefore, it creates significant challenges in anomaly detection in such complicated systems. How to apply such deep learning methods for real-time spatio-temporal metamodeling and anomaly detection has not been fully discussed yet in literature, especially for cardiac electrical simulation. More discussions will be provided in Section 2.

In this paper, we will focus on developing a new deep spatio-temporal sparse decomposition (DSTSD) method, which combines the power of the deep neural network to represent the complicated spatio-temporal patterns of the mean trend and the decomposition framework to separate the sparse anomaly from the mean

trend. More specifically, two spatio-temporal model architectures are combined into the proposed DSTSD, namely the ConvLSTM and ConvWaveNet, for metamodeling and model the nonlinear dynamics of the cardiac electric conduction. We demonstrate that in the case of highly nonlinear spatio-temporal systems, the proposed DSTSD method can achieve both the smallest detection delay and accurate localization of the anomaly.

In conclusion, the rest of the paper is organized as follows. Section 2 reviews the related literature in cardiac electrical conduction modeling and spatio-temporal anomaly detection. Section 3 gives the motivating example of our study for transmembrane potential simulation. Section 4 introduces the proposed DSTSD methodology for spatio-temporal metamodeling, spatio-temporal mean trend prediction, and anomaly detection. Section 5 shows the simulation study to demonstrate the performance of the proposed method for both long-term prediction and anomaly detection. Section 6 concludes the paper with future work.

## 2 Literature Review

In this section, we will first review the literature on modeling and anomaly detection of Cardiac Electrical Conduction. We will then review some data-driven methodology on the monitoring and diagnosis of spatio-temporal data.

### 2.1 Cardiac Electrical Conduction Modeling and Anomaly Detection

Modeling and analysis of irregular cardiac electrical conduction have been widely studied in the literature, including the efficient numerical simulation model [9, 10]. To detect anomalies in such complex spatio-temporal systems, we briefly classified the current methodology applied to the cardiac electrical conduction Modeling into model-based, metamodel-based and statistical-based methodology.

In the first category, most of the works have been focused on using a model-based control method to control the anomaly [11]. For example, Garzon et al. [12] proposed a model-based continuous-time feedback control methodology to suppress the anomaly. Marcotte and Grigoriev [13] proposed an adjoint eigenfunction method to provide localization for the dynamics and control of the unstable spiral wave. Some efforts to reduce the computational complexity, including Galerkin projection [12] and numerical approximation [10] have been proposed. However, the major limitations of the model-based methodology are that these models require all the complex dynamic models and parameters to be known, which may not be feasible in practice.

In the second category, metamodeling has been a popular approach that helps reduce model complexity with unknown dynamics models and overcome computational challenges. Gaussian Process (GP) model has been a popular choice to extract information from high-dimensional data. Especially, the GP model is widely

used to model the shape of the action potential [14, 15, 16]. However, the major limitation of GP models is that GP models lack the ability to perform long-term prediction and are often computationally inefficient, which is not a good candidate for metamodeling and real-time anomaly detection purpose.

In the third category, machine learning methods are applied to detect irregular behavior. For example, Yang et al. [17] proposed a classification model by combining a feature embedding technique and a self-organizing map to classify different types of myocardial infarction. For unknown anomaly detection, Loppini et al. [18] proposed to use the statistical correlation functions to detect irregular behaviors. Greisas et al. [19] proposed to Principal Component Analysis (PCA) for the detection of abnormal cardiac activity. However, without a good metamodel, it is often hard to accurately infer the time, location, and magnitude of the external stimulation.

## 2.2 Spatio-temporal Anomaly Detection Literature

Here, we will review some data-driven methodology on the monitoring and diagnosis of spatio-temporal data. Current research in this area can be classified into three groups: principal component analysis-based approach, functional data analysis-based techniques, and deep learning-based methods.

In the first group, principal component analysis (PCA) is one of the most popular methods for spatio-temporal data dimension reduction because of its simplicity, scalability, and data compression capability. For example, PCA [20], multivariate functional PCA [21], tensor-based decomposition method [22], multi-resolution PCA [23], subspace learning [24] have been proposed to reduce the dimensionality and then apply the control chart on the low-dimensional embedding and the residual space. The main drawback of current PCA-based methods is that they cannot be directly used for spatio-temporal data streams with a time-varying mean.

The second category attempts to model the spatio-temporal data as functional data by modeling the data structure by a set of known spatial or temporal basis, kernel, and covariance structure. For example, non-parametric methods based on local kernel regression [25, 26, 27], splines [28] and wavelets [29] are proposed. Other works such as longitudinal data analysis [30, 31], Gaussian process [32] are also proposed. However, these methods do not directly model the structure of the anomaly. Therefore, decomposition-based approaches have become popular due to the ability to decompose the anomaly signals directly from the complex spatio-temporal trend [8]. However, one major drawback of the decomposition method is that these methods assume the spatio-temporal data can be represented by a set of known basis or kernels, which failed to model the complicated spatio-temporal structure of the signal.

To monitoring complicated spatio-temporal systems, deep learning methods such as convolutional neural

networks and generative adversarial networks have been applied. We can divide the current literature for deep learning in spatio-temporal anomaly detection into two classes: Unsupervised autoencoder approaches and supervised spatio-temporal regression. For the autoencoder approaches, spatio-temporal autoencoders [33] and Generative Adversarial Nets [34] have been proposed to detect anomalous events. The autoencoder approaches can dramatically reduce the dimensionality of the original problems, and the monitoring statistic is often defined as a function of the model residual. In literature, prediction-based deep learning methods have also been used for anomaly detection. For example, feed-forward convolutional networks are proposed in [35] for video prediction by minimizing the mean square error of future prediction. Another deep learning framework for anomaly detection [36] utilizes the unsupervised learning method to extract features and then detect irregularities through a prediction system. For either supervised and unsupervised anomaly detection problems in literature, no existing works exist to separate the anomaly signals from the original spatio-temporal mean trend.

### 3 Motivating Study: Electrical Propagation Through One-dimensional Cell String based on Courtemanche-Ramirez-Nattel (CRN) Model

In this study, Courtemanche-Ramirez-Nattel (CRN) model [4] was used to simulate the transmembrane potential of individual cardiac cells. CRN model is a detailed model that describes the complex mechanism of cardiac electrical signaling in human atrial cells. The mono-domain tissue model is adopted to simulate the electrical wave propagation on a one-dimensional (1D) cell string. CRN model is a physiologically realistic model for human atrial cells, which provides a detailed description of ionic channel gating. More specifically, it models the complex spatio-temporal dynamics of transmembrane potential, which is defined as the difference in the electric potential between the interior and the exterior of the biological cell, by partial differential equations (PDE) defined in (1).

$$\frac{\partial u(t, s)}{\partial t} = -\frac{I_{ion}(u(t, s), \mathbf{v}(t, s))}{C_m} + D\frac{\partial^2 u(t, s)}{\partial s^2} + c(t, s) \quad (1)$$

$$\frac{\partial v(t, s)}{\partial t} = h(u(t, s), \mathbf{v}(t, s)). \quad (2)$$

Here,  $t$  represents time and  $s$  indicates spatial location.  $u(t, s)$  is the transmembrane potential,  $\mathbf{v}(t, s)$  is a vector of variables associated with the ion channel conductance (gating variables).  $c(t, s)$  is the external stimulus,  $C_m$  is the total capacitance, and  $D$  is the isotropic diffusion coefficient determined by gap junction

resistance, surface-to-volume ratio, and membrane capacitance [4].  $I_{ion}$  is the summation of 12 different ion channel currents, which are controlled by  $u(t, s)$  and  $\mathbf{v}(t, s)$  with over 70 equations. These equations are compactly represented by  $h(u(t, s), \mathbf{v}(t, s))$  in (2), and their detailed expressions as well as model parameters used for the data generation can all be found in [3]. In reality, the transmembrane potential  $u(t, s)$  can often be measured (i.e., observable), but the ion currents  $I_{ion}$  and the associate hidden variable  $\mathbf{v}(t, s)$  are often hard to obtain (i.e., unobservable). Although  $I_{ion}$  and  $\mathbf{v}(t, s)$  are unobservable, it is known that they take into effect on the transmembrane potential within different periods, such as the sodium currents affect the rising of  $u(t, s)$  while potassium currents influence its restoration. It is such a phenomenon that motivates the proposed modeling structure in the next section. The CRN model has been popularly used in many studies to simulate both normal heart functions and cardiac disorders such as atrial fibrillation [37, 3, 38]. However, due to its computational complexity, metamodeling techniques are important to reduce computational complexity. The details of the CRN model can be found in [4].

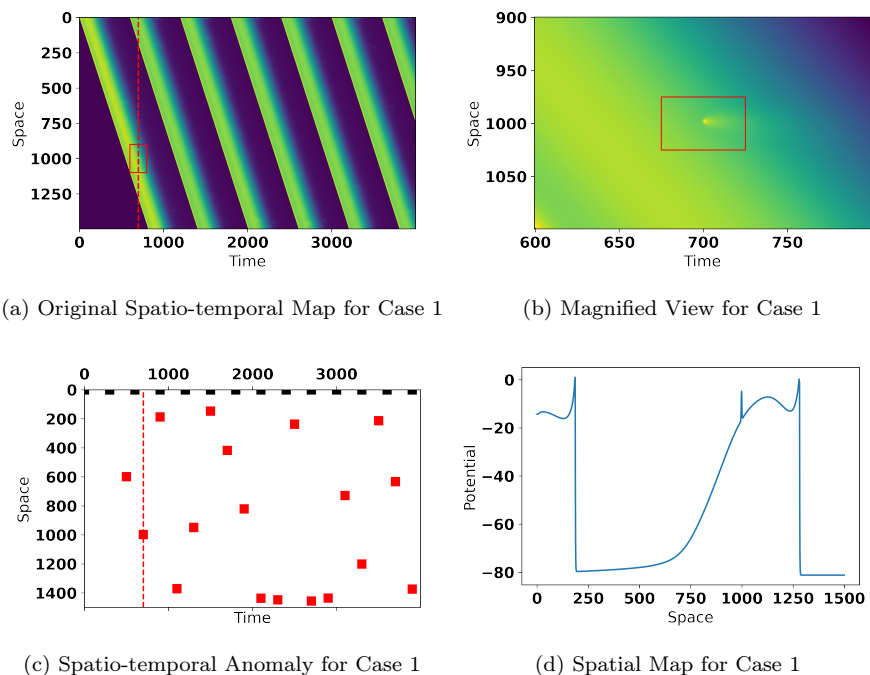


Figure 1: Here shows the data generated by the CRN model with a single stimulation at the 1<sup>st</sup> cell. The X axis and Y axis in Fig. 1a, Fig. 1c and Fig. 1b represent time and space (cell) index correspondingly. The X axis and Y axis in Fig. 1d represent space (cell) index and the magnitude of cell potential. Fig. 1a describes the raw signal in a 2D plot. It shows the magnitude of the potential at different spatial-temporal locations. Fig. 1d is an example of potential along with the cells at  $t = 700$ . Fig. 1c describes the stimulation where regular stimulation is marked in black, and abnormal stimulation is marked in red. For Case I, there are repeated normal stimulation at the 1<sup>st</sup> cell and the abnormal stimulation happens randomly along the cells. Fig. 1b visualize one example of abnormal stimulation at  $t = 700$

Fig. 1 and Fig. 2 show two different simulations of the spatio-temporal propagation on a one-dimensional

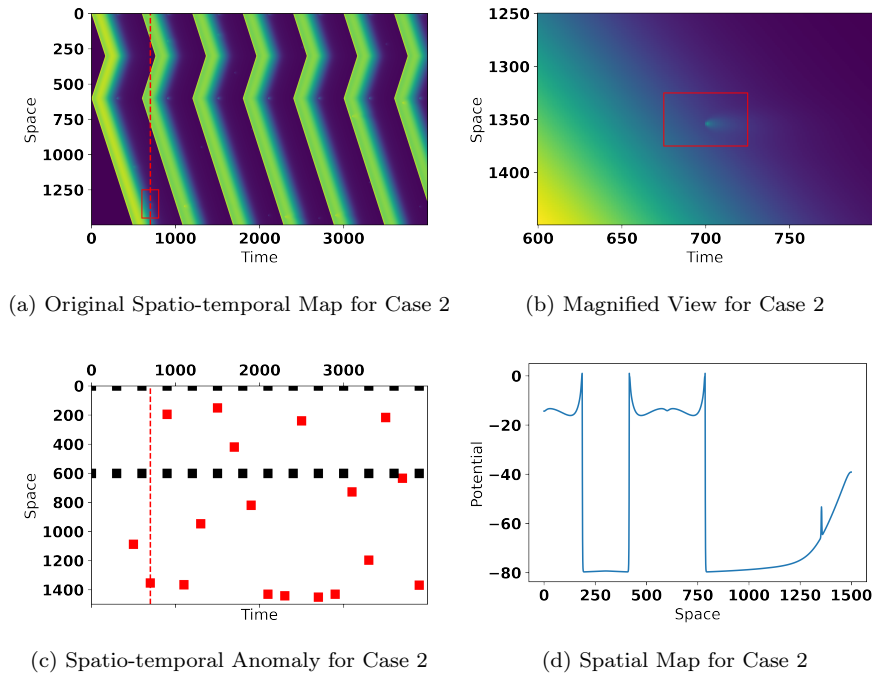


Figure 2: Here shows the data generated by the CRN model with two stimulation at the 1<sup>st</sup> cell and the 600<sup>st</sup> cell. Fig. 8a describes the raw signal in a 2D plot. Fig. 9b is an example of potential along with the cells at  $t = 700$ . Fig. 9a describes the stimulation where regular stimulation is marked in black, and abnormal stimulation is marked in red. Fig. 8b visualize one example of abnormal stimulation at  $t = 700$

cell string consisting of 1500 cells. The horizontal axis shows the propagation time in milliseconds, and the vertical axis shows the cell index. Periodic stimulation is given to the 1st cell in the first case and to the 1st and 600th cells in the second case. Fig. 1a and Fig. 8a show the spatio-temporal map of transmembrane potentials. Fig. 1b and Fig. 8b show the magnified spatio-temporal 2D map between 600ms and 800ms around the anomaly regions (between the 1250th cell and the 1500th cell). The anomalies at  $t = 700$  are highlighted by red squares. Further, Fig. 1c and Fig. 9a mark the regular and abnormal stimulation, and Fig. 1d and Fig. 9b show the 1D spatial map around these anomaly regions (i.e., the transmembrane potentials along the cell string).

In both cases, every other stimulation dies out and does not propagate like others. This is due to the refractoriness of the cardiac cell, where immediate stimulation after repolarization within in the cell refractory period cannot be initiated. The refractoriness of the cardiac cell can change the propagating direction when two waves merge together, as seen in the right case. It is essential to model such refractoriness to capture the complex and dynamic activities of cardiac electrical waves. Besides the regular stimulation, there are also signals caused by irregular stimulations due to the malfunction of the cardiac cells.

The goals of this paper are to 1) develop a metamodeling framework to learn the nonlinear spatio-temporal



dynamics from the data/observations and apply it to predict the spatio-temporal conduction of electrical waves in future times. Here, the CRN model will be used as a case study to test and validate the proposed method. However, the proposed metamodeling framework can be generally applied to other spatio-temporal systems as well and greatly improve computational efficiency without losing too much accuracy. 2) given the metamodel, design a real-time anomaly detection strategy to localize and separate the abnormal stimulation (i.e., anomaly) automatically from incoming observations.

## 4 Methodology

In this subsection, the proposed deep spatio-temporal sparse decomposition (DSTSD) method is introduced in Section 4.1. We will then discuss two deep spatio-temporal architectures that are useful to model the complicated spatio-temporal structure in Section 4.2, namely the convolutional WaveNet (Conv-WaveNet), and convolutional long short-term memory (Conv-LSTM). In addition, to optimize the deep learning algorithm in the presence of the outlier, we proposed a robust spatio-temporal learning procedure, which estimates the parameters of DSTSD in Section 4.3. In Section 4.4, we discuss how the trained DSTSD can be used to achieve long-term prediction of the spatio-temporal mean trend. In Section 4.5, we proposed to through solving the inverse problem through a buffer-window approach to give a more accurate estimation of the anomaly. In Section 4.6, the estimated anomaly will be used to conduct a likelihood ratio test to give an alarm as soon as the anomaly is detected. Finally, in Section 4.7, we introduce procedures for the selection of tuning parameters.

Finally, in this paper, we will use non-bold symbols to represent scalar, bold symbol  $\mathbf{a}$  to represent vectors, capital bold symbol  $\mathbf{A}$  to represent matrices. For a more detailed notation table, please see the online Appendix.

### 4.1 Deep Spatio-Temporal Sparse Decomposition

In this paper, we focus on the modelling of complicated nonlinear spatio-temporal dynamics in the HD (high dimensional) data streams. For simplicity, we begin with profile data and suppose a sequence of profiles  $\{\mathbf{y}_i\}_{i=1}^n$  are available at  $n$  different time instances  $\tau = [\tau_1, \dots, \tau_n]^T$ . For each profile, we assume the observations are taken at the same group of  $p$  spatial locations, denoted as  $\mathbf{x} = [x_1, \dots, x_p]^T$ . It is worth noting that the observation locations can vary for different profiles and it does not introduce any complexity to the implementation of the proposed method. Then, for the  $i^{th}$  profile, we have  $\mathbf{y}_i = [y(\tau_i, x_1), \dots, y(\tau_i, x_p)]^T$ . In addition, the  $i^{th}$  profile is assumed to be decomposed as  $\mathbf{y}_i = \boldsymbol{\mu}_i + \mathbf{e}_i$ , where  $\boldsymbol{\mu}_i = [\mu(\tau_i, x_1), \dots, \mu(\tau_i, x_p)]^T$  is the mean trend and  $\mathbf{e}_i = [e(\tau_i, x_1), \dots, e(\tau_i, x_p)]^T$  represents the observation noise. Thus, the objective

of this research is to infer the dynamics governing  $\mu(t, s)$  for long-term prediction and anomaly detection. However, due to the complexity of the underlying mechanism and the scarcity of the available information, this is difficult to be accomplished using basic modelling approaches. For example, suppose we are interested in estimating the dynamics of transmembrane potential, that is,  $\mu(t, s) = u(t, s)$ . As described in section 3,  $u(t, s)$  is the only variable that can be observed, whose evolution is collectively regulated by a bunch of unobserved variables, i.e.,  $I_{ion}$  and  $\mathbf{v}(t, s)$ , through lots of nonlinear equations. These special features complicate the estimation of the underlying dynamics of  $u(t, s)$ . Therefore, we introduce a deep spatio-temporal sparse decomposition (DSTSD) structure to achieve the research goal.

To learn the complex dynamics, the evolution of  $\mu(t, s)$  at location  $x_q$  is assumed to be governed by the following equation:

$$\mu(\tau_{i+1}, x_q) = \mu(\tau_i, x_q) + f(\{\boldsymbol{\mu}_j\}_{j \leq i}) + \mathbf{c}_{i+1}. \quad (3)$$

This assumption indicates that the difference of the mean trend at a specific location, i.e.,  $\mu(\tau_{i+1}, x_q) - \mu(\tau_i, x_q)$ , is controlled by two components. The first component  $f(\cdot)$  is a complicated function to be modeled using a neural network, which takes the historical trajectories at all  $p$  locations as inputs. Introducing the mean at other locations is to model the interaction among different spatial locations. The intuition for incorporating historical information of  $\mu(t, s)$  in the dynamics is based on the observation of the CRN model. As mentioned in section 3, the unobservable take into effect the transmembrane potential within different time periods. Thus, the information within the former can be extracted from the historical information of the latter, i.e.,  $\{\boldsymbol{\mu}_j\}_{j \leq i}$ . The second component  $\mathbf{c}_i = [c(\tau_i, x_1), \dots, c(\tau_i, x_p)]^T$  is the external stimulation exerted on the system. To detect the anomaly, we assume that the stimulation at time  $\tau_i$  can be decoupled as  $\mathbf{c}_i = \mathbf{r}_i + \mathbf{a}_i$ , where  $\mathbf{r}_i$  is the regular stimulation as shown in black in Fig. 1c, and  $\mathbf{a}_i$  is the abnormal stimulation as shown in red in Fig. 1c.

In reality, we can not directly use (3) to estimate  $\mu_{i+1}$  given  $\{\boldsymbol{\mu}_j\}_{j \leq i}$  for the following two reasons: 1) the system dynamic  $f(\cdot)$  is often unknown. 2) We only have noisy observations of  $\{\boldsymbol{\mu}_i\}_{i=1}^n$ , i.e.,  $\{\mathbf{y}_i\}_{i=1}^n$ . To estimate  $\{\boldsymbol{\mu}_i\}_{i=1}^n$  given  $\{\mathbf{y}_i\}_{i=1}^n$  without knowing the system dynamics  $f(\cdot)$ , we propose another function  $g(\cdot)$ , which can take the noisy observation  $\{\mathbf{y}_i\}_{j \leq i}$  as input to estimate the system dynamics. To put it simply,  $g(\cdot)$  estimate the differences of  $\boldsymbol{\mu}_{i+1} - \boldsymbol{\mu}_i$ . In addition, to better capture the abnormal stimulation, a spatial basis  $\mathbf{B}_a$  is assumed to be existed to decompose  $\mathbf{a}_i$  as  $\mathbf{a}_i = \mathbf{B}_a \boldsymbol{\theta}_{a,i}$ , where  $\boldsymbol{\theta}_{a,i}$  are the temporal coefficients of the anomaly at time  $\tau_i$ . The spatial basis of the anomaly should represent the spatial structure of the anomaly. Here, we assume that the anomaly is a local clustered region, therefore, a spline basis is used. To put things together, we can have (4):

$$\mathbf{y}_{i+1} = \boldsymbol{\mu}_i + g(\{\mathbf{y}_j\}_{j \leq i}; \boldsymbol{\theta}) + \mathbf{r}_{i+1} + \mathbf{B}_a \boldsymbol{\theta}_{a,i+1} + \mathbf{e}_{i+1}. \quad (4)$$

where  $\boldsymbol{\theta}$  is the parameters of function  $g(\cdot)$ . Although the proposed structure is motivated by the CRN model, we would like to emphasize that it is very general and can be applied for other spatio-temporal dynamics.

To estimate  $\boldsymbol{\theta}$ , and  $\boldsymbol{\theta}_{a,i}$ , we propose a penalized regression model to estimate all the parameters through the following loss function

$$\begin{aligned} l(\boldsymbol{\theta}, \boldsymbol{\theta}_{a,i+1}) = & \sum_{i=1}^n \|\mathbf{y}_{i+1} - g(\{\mathbf{y}_j\}_{j \leq i}; \boldsymbol{\theta}) - \boldsymbol{\mu}_i \\ & - \mathbf{B}_a \boldsymbol{\theta}_{a,i+1} - \mathbf{r}_{i+1}\|^2 \\ & + \lambda \boldsymbol{\mu}_i^T \mathbf{R} \boldsymbol{\mu}_i + \gamma \|\boldsymbol{\theta}_{a,i+1}\|_1, \end{aligned} \quad (5)$$

where  $\|\cdot\|_1$  is the  $L_1$  norm operator, and  $\lambda$  and  $\gamma$  is the tuning parameter to be determined by the user.  $\lambda \boldsymbol{\mu}_i^T \mathbf{R} \boldsymbol{\mu}_i$  encourages the smoothness of background and  $\gamma \|\boldsymbol{\theta}_{a,i}\|_1$  encourage the sparsity of the anomalous regions. The Matrix  $\mathbf{R}$  is the regularization matrix that controls the smoothness of the mean function  $\boldsymbol{\mu}_i$ . For example, one popular choice for  $\mathbf{R}$  is that  $\mathbf{R} = \mathbf{D}^T \mathbf{D}$ , where  $\mathbf{D}$  is the second-order differential operator

$$\text{as } \mathbf{D} = \begin{bmatrix} 1 & -2 & 1 & & \\ & \ddots & \ddots & & \\ & & 1 & -2 & 1 \\ & & & \ddots & \ddots \\ & & & & 1 & -2 & 1 \end{bmatrix}.$$

Therefore, in the following chapters, we will first discuss two variants of the spatio-temporal model architectures  $g(\cdot)$  for the spatial-temporal mean trend of the functions and then discuss how to estimate  $\boldsymbol{\mu}_i$  in the current framework.

## 4.2 Spatio-temporal Model Architectures for $\boldsymbol{\mu}_t$

In this subsection, we will evaluate two popular deep learning architectures for the complex spatio-temporal dynamic models  $g(\{\mathbf{y}_j\}_{j \leq i}; \boldsymbol{\theta})$  in (4), inspired by the CRN equation in (1). In literature, there are many spatio-temporal models that can be used. Here, we are specifically interested in nonlinear methods with long-term prediction capacity. We will also evaluate which model is able to predict the refractoriness effect of cardiac cells. More specifically, we will focus on two specific models Convolutional WaveNet (Conv-WaveNet) and Convolutional Long Short-Term Memory Networks Model (Conv-LSTM) due to their ability to model the long-term dependency. More details about the specific architecture are discussed in the supplementary material.

#### 4.2.1 Convolutional WaveNet (Conv-WaveNet)

WaveNet was originally introduced to model and generate realistic audio waveforms by considering the long-term dependency of the time sequence by the use of deep dilated convolution to increase the receptive field to model long-term dependency. We propose to extend the WaveNet architecture with spatial convolution such that the complex spatial correlation and long-term dependency can be modeled simultaneously[39]. Here, we denote the size of the receptive window as  $w_r$ .

$$g(\{\mathbf{y}_j\}_{j \leq t}; \boldsymbol{\theta}) = g(\mathbf{y}_{t-w_r:t}; \boldsymbol{\theta})$$

Therefore,  $g(\mathbf{y}_{t-w_r:t}; \boldsymbol{\theta})$  is a function of  $\mathbf{y}_{t-w_r}, \mathbf{y}_{t-w_r+1}, \dots, \mathbf{y}_t$ . Here, the receptive field  $w_r = 2^d$ , where  $d$  is the number of dilated convolutional layers in the deep neural network. The benefit of using the WaveNet architecture is that the receptive field increases exponentially with the depth so that the long-term dependency can be modeled. More details about the Conv-WaveNet architecture are discussed in the supplementary material.

#### 4.2.2 Convolutional Long Short-Term Memory Networks Model (Conv-LSTM)

LSTM is one type of recurrent neural network that is designed to learn the long-term dependencies. They are widely used in a large variety of problems, such as time-series prediction and natural language processing. However, the LSTM method is not suitable to model the spatio-temporal propagation since it uses the fully connected transition matrices on the hidden state, which cannot take advantage of the spatial neighborhood structure during the temporal transition and could potentially lead to the overfitting [40]. In contrast, Conv-LSTM is proposed in [40] to model this local propagation via the convolutional operator. We use  $\mathbf{z}_{h_t}$  to represent the memory state of Conv-LSTM at time  $t$  and Conv-LSTM is a recursive function to link the data and previous memory state as:

$$\begin{aligned} \mathbf{z}_{f_t} &= \sigma_g(\boldsymbol{\theta}_{W_f} * \boldsymbol{\mu}_t + \boldsymbol{\theta}_{U_f} * \mathbf{z}_{h_{t-1}} + \boldsymbol{\theta}_{V_f} \circ \mathbf{z}_{c_{t-1}} + b_f) \\ \mathbf{z}_{i_t} &= \sigma_g(\boldsymbol{\theta}_{W_i} * \boldsymbol{\mu}_t + \boldsymbol{\theta}_{U_i} * \mathbf{z}_{h_{t-1}} + \boldsymbol{\theta}_{V_i} \circ \mathbf{z}_{c_{t-1}} + b_i) \\ \mathbf{z}_{c_t} &= \mathbf{z}_{f_t} \circ \mathbf{z}_{c_{t-1}} + \mathbf{z}_{i_t} \circ \sigma_c(\boldsymbol{\theta}_{W_c} * \boldsymbol{\mu}_t + \boldsymbol{\theta}_{U_c} * \mathbf{z}_{h_{t-1}} + b_c) \\ \mathbf{z}_{o_t} &= \sigma_g(\boldsymbol{\theta}_{W_o} * \boldsymbol{\mu}_t + \boldsymbol{\theta}_{U_o} * \mathbf{z}_{h_{t-1}} + \boldsymbol{\theta}_{V_o} \circ \mathbf{z}_{c_{t-1}} + b_o) \\ \mathbf{z}_{h_t} &= \mathbf{z}_{o_t} \circ \sigma_h(\mathbf{z}_{c_t}) \\ \boldsymbol{\mu}_{t+1} &= \boldsymbol{\mu}_t + \mathbf{z}_{h_t} + \mathbf{c}_{t+1} \end{aligned}$$

Again, motivated by the Euler’s equation, the LSTM model is used to model the difference between  $\mu_t$  and  $\mu_{t+1}$ . Here, we use  $\mathbf{z}_{f_t}, \mathbf{z}_{i_t}, \mathbf{z}_{c_t}, \mathbf{z}_{o_t}, \mathbf{z}_{h_t}$  to denote the latent state variables, namely the forget gate, input gate, cell state, output gate, and hidden state inside the LSTM model, and we use  $\boldsymbol{\theta}_{W_f}, \boldsymbol{\theta}_{U_f}, \boldsymbol{\theta}_{V_f}, \boldsymbol{\theta}_{W_i}, \boldsymbol{\theta}_{U_i}, \boldsymbol{\theta}_{V_i}, \boldsymbol{\theta}_{W_c}, \boldsymbol{\theta}_{U_c}, \boldsymbol{\theta}_{V_c}, \boldsymbol{\theta}_{W_o}, \boldsymbol{\theta}_{U_o}, \boldsymbol{\theta}_{V_o}$  to denote the parameters for LSTM model [40], which are the parameters for the forget gate, input gate, cell state, and output gate, respectively. Notation  $\circ$  represents the Hadamard product and  $*$  represents the convolution operator.

### 4.3 Phase-I Analysis

In the Phase-I analysis, we will discuss the algorithm to optimize  $\boldsymbol{\theta}$  and  $\boldsymbol{\theta}_{a,t}$  in the off-line setting for Phase-I analysis. We assume that a set of spatio-temporal data  $y_{i,t}$  with length  $N_t$  will be collected with  $i = 1, \dots, N$ . To simplify the cases, we assume that the outliers in Phase-I analysis, if exist, are often random, which corresponds to  $\mathbf{B}_a = \mathbf{I}$ .

We first prove that solving  $\boldsymbol{\theta}$  and  $\boldsymbol{\theta}_a$  in (5) is equivalent to optimize the  $\boldsymbol{\theta}$  with the Huber loss function in the following proposition and then the soft thresholding on the residual.

**Proposition 1.** *When  $\mathbf{B}_a = \mathbf{I}$ , in (5),  $\boldsymbol{\theta}$  can be solved by*

$$\boldsymbol{\theta} = \arg \min_{\boldsymbol{\theta}} l_r(\boldsymbol{\theta}) \quad (6)$$

$$\boldsymbol{\theta}_{a,i,t+1} = S_{\gamma/2}(\mathbf{y}_{i,t+1} - g(\{\mathbf{y}_{i,t'}\}_{t' \leq t}; \boldsymbol{\theta}) - \boldsymbol{\mu}_{i,t} - \mathbf{r}_{t+1}), \quad (7)$$

where  $l_r(\boldsymbol{\theta})$  is defined as:

$$l_r(\boldsymbol{\theta}) = \sum_{i=1}^N \sum_{t=1}^{N_t} (\rho(\mathbf{y}_{i,t+1} - g(\{\mathbf{y}_i\}_{i \leq t}; \boldsymbol{\theta}) - \boldsymbol{\mu}_t - \mathbf{r}_{t+1}) + \lambda \boldsymbol{\mu}_t^T \mathbf{R} \boldsymbol{\mu}_t). \quad (8)$$

Here,  $\rho(x)$  is the Huber loss function, defined by  $\rho(x) = \begin{cases} x^2 & |x| \leq \frac{\gamma}{2} \\ \gamma|x| - \frac{\gamma^2}{4} & |x| > \frac{\gamma}{2} \end{cases}$ .  $S_{\gamma}(x) = \text{sgn}(x)(|x| - \gamma)_+$

is the soft thresholding operator, in which  $\text{sgn}(x)$  is the sign function and  $x_+ = \max(x, 0)$ .

The proof is given in the Supplementary Material.

Finally, given the loss function in (8), the parameter  $\boldsymbol{\theta}$  can be solved by the combination of the back-propagation and the stochastic gradient descent to update the model parameter  $\boldsymbol{\theta}$  based on a mini-batch of samples in the  $k^{\text{th}}$  iteration. More specifically, in the Conv-WaveNet model, since  $g(\{\mathbf{y}_i\}_{i < t}; \boldsymbol{\theta}) = g(\mathbf{y}_{t-w_r:t}; \boldsymbol{\theta})$ ,  $\frac{g(\mathbf{y}_t; \boldsymbol{\theta})}{\partial \boldsymbol{\theta}}$  can be directly computed via the back-propagation. However, for the Conv-LSTM

model, the gradient will flow back into the starting time, which increases the computational complexity dramatically for large  $t$ . Normally, truncated back-propagation can be applied to cut the gradient flow in the latest few measurements to decrease the computational complexity.

#### 4.4 Real-time Long-term Prediction

The previous subsection focuses on training the spatio-temporal models in the off-line setting. However, since the temporal dimension is changing over time, it is not trivial to apply the model in the online-setting for real-time long-term prediction. In the example of the cardiac electric conduction, it is important to predict the future events in a couple of cardiac cycles (i.e, heartbeats) for over 500ms to 1000ms ( $\Delta t = 0.1\text{ms}$ ). In the anomaly detection application, the long-term prediction provides references to identify abnormal stimulation. To achieve this, we will discuss how to apply the trained model in the online setting in real-time.

In this subsection, we will discuss how to enable the long-term prediction for both Conv-WaveNet models and Conv-LSTM models. However, since the temporal dependency of these two models is different, we will discuss them separately as follows:

**Conv-WaveNet:** We will discuss how to enable the long-term prediction for the Conv-WaveNet model. Here, we denote  $\boldsymbol{\mu}_{t_0}(t_0 + \Delta t)$  as the  $\Delta t$ -ahead prediction of  $\boldsymbol{\mu}(t_0 + \Delta t)$  at time  $t_0$ . For the long-term prediction, the following method can be used. We know that  $\hat{\boldsymbol{\mu}}(t_0 + i + 1) = \mathbf{c}_{t_0+i+1} + \hat{\boldsymbol{\mu}}(t_0 + i) + g(\mathbf{y}_{t_0+i-w_r:t_0+i}; \boldsymbol{\theta})$ . Therefore, we can derive the following formula for the long-term prediction.

$$\hat{\boldsymbol{\mu}}_{t_0}(t_0 + \Delta t) = \mathbf{y}_{t_0} + \sum_{i=1}^{\Delta t-1} g(\hat{\boldsymbol{\mu}}_{t_0+i-w_r:t_0+i}; \boldsymbol{\theta}) + \mathbf{c}_{t_0+\Delta t}$$

Here, typically, in the real-time prediction, we will set the future anomaly  $\mathbf{a}_t = 0$ . However, in some rare cases, the future anomaly source is already known  $\mathbf{a}_t$ , this method can also predict how the system reacts to the anomaly accurately.

**Conv-LSTM:** Similarly, we would like to discuss how to enable long-term prediction for the Conv-LSTM model. Unlike the Conv-WaveNet model, the predicted value  $\hat{\boldsymbol{\mu}}_{t_0}(t_0 + 1)$  requires all values  $\mathbf{y}_t, t = 1, \dots, t_0$ . We divide the long-term prediction into two phases: the warm-up phase and the prediction phase. In the warm-up phase, we will start with  $y_0$  or some value from  $\mathbf{y}_{t'}, t' < t_0$  to learn a more accurate memory state representation  $h_t$  from the original data as well as estimating the mean trend  $\boldsymbol{\mu}_t$  in the past. In the warm-up phase, the  $\mathbf{y}_t$  is known for  $t = 1, \dots, t_0$ , therefore,  $\mathbf{y}_t$  can be used as input for the Conv-LSTM model. Furthermore,  $\hat{\mathbf{a}}_{t+1} = \hat{\boldsymbol{\theta}}_{a,t+1}$  in the phase-I analysis, can be estimated by (7). In the prediction phase,  $\mathbf{y}_t$  is not known for  $t > t_0$ . In this case, we propose to use the future prediction  $\hat{\boldsymbol{\mu}}_t$  for  $t > t_0$ . In the long-term prediction phase, if we know the future stimulation  $\mathbf{a}_t$ , this can be combined in future prediction. If we do

not know where and when the future stimulation is, we typically set  $\mathbf{a}_t = 0$ .

## 4.5 Online Anomaly Estimation

In this subsection, we will discuss how to apply the proposed algorithm for online anomaly detection. More specifically, we assume that the anomaly is sparse and only happens at a certain time interval  $t \in [T_0, T_0 + w]$  (i.e., epidemic change [41]). This type of change is very common in the cardiac electrical conduction. Mathematically speaking, we define the normal and abnormal transition in (9).

$$\begin{aligned} \boldsymbol{\mu}_{t+1}(s) &= \boldsymbol{\mu}_t(s) + f(\boldsymbol{\mu}_t(s)) + \mathbf{r}_{t+1}, t < T_0 \text{ or } t > T_0 + T_w \\ \boldsymbol{\mu}_{t+1}(s) &= \boldsymbol{\mu}_t(s) + f(\boldsymbol{\mu}_t(s)) + \mathbf{r}_{t+1} + \mathbf{a}_{t+1}, t \in [T_0, T_0 + T_w], \end{aligned} \quad (9)$$

Detecting the epidemic change is very challenging. The reason is that if we design a control chart methodology only based on the Q-control chart, designed based on the model residual such as  $Q(t) = \|\mathbf{y}_t - \boldsymbol{\mu}_{t-1} - g(\{\mathbf{y}_{t'}\}_{t' < t-1}; \boldsymbol{\theta})\|^2$ ,  $Q(t)$  will be small for  $t < T_0$  or  $t > T_0 + T_w$  and only be large during the epidemic change window  $[T_0, T_0 + T_w]$ . Therefore, if the algorithm fails to detect the anomaly at time  $t \in [T_0, T_0 + T_w]$ , it may never detect the anomaly again in the future time  $t' > T_0 + T_w$  since the anomaly will be combined into the future spatio-temporal mean trend in the next time as  $\boldsymbol{\mu}_t = \boldsymbol{\mu}_{t-1} + g(\{\mathbf{y}_{t'}\}_{t' < t-1}; \boldsymbol{\theta}) + \mathbf{a}_t$  and results in small residual  $Q(t)$  for future  $t' > T_0 + T_w$ .

Another aspect is that when the anomaly happens at time  $T_0$ , it will start with a small magnitude at  $T_0$  and then propagate to a large area in the future time  $t > T_0$ . Therefore, it is often much effective to detect such change from a retrospective perspective to analyze the change point and location that may happen in the past. However, a full perspective requires scanning all possible locations of changes back in time, which is computationally inefficient.

To address this, we propose to use a buffer window to provide a better estimation of the anomaly event. Suppose we would like to detect change at time  $T$ , we propose to use  $T+w$  to  $T$  as a buffer period to estimate the source of the anomaly. This may naturally introduce a detection delay due to the buffer window  $w$  but will create a better estimation of the anomaly. For a special case,  $w = 0$ , only data  $y_T$  will be used to detect the change at time  $T$ . For more discussion about choosing the best buffer period, please refer to Section 4.7.

This procedure relies on the long-term prediction capacity of the proposed algorithm. For example, we assume that under this buffer period, the true data  $\mathbf{y}_t$  is not measured. Therefore, to estimate the change, we have to rely on the predicted  $\boldsymbol{\mu}_t$  when  $t > T$ . Therefore, we have:

$$\begin{aligned} \boldsymbol{\mu}_{t+k} &= \boldsymbol{\mu}_{t+k-1} + g(\{\boldsymbol{\mu}_{t'}\}_{t \leq t' < t+k}; \boldsymbol{\theta}) + \mathbf{a}_{t+k} + \mathbf{r}_{t+k} \\ \text{s.t. } k &= 1, \dots, w. \end{aligned} \quad (10)$$

Furthermore, in Phase-II monitoring, we assume that the spatio-temporal model has been trained before, and  $\boldsymbol{\theta}$  has to be estimated. We will rely on the following optimization algorithms to estimate the  $\boldsymbol{\theta}_{a,t}$ . Here, one specific challenge is the recursive formula of  $g$ . Since  $\boldsymbol{\mu}_t$  relies on  $\boldsymbol{\mu}_{t-1}$ , which in turns relies on  $\mathbf{a}_{t-1}$ . Therefore, the following loss function aims to optimize or estimate the anomaly from time  $T$  to  $T+w$ , namely  $\mathbf{a}_T$  to  $\mathbf{a}_{T+w}$ . The challenge is that the problem is highly coupled, given the recursion of  $\boldsymbol{\mu}_{t+k}$ , as shown in (11).

$$\min_{\{\boldsymbol{\theta}_{a,t}\}_{t \in [T, T+w]}} \sum_{t=T}^{T+w} \|\mathbf{y}_t - \boldsymbol{\mu}_t\|^2 + \gamma \sum_{t=T}^{T+w} \|\boldsymbol{\theta}_{a,t}\|_1 \quad (11)$$

$$\begin{aligned} \text{s.t. } \boldsymbol{\mu}_{T+w} &= \boldsymbol{\mu}_{T+w-1} + g(\{\boldsymbol{\mu}_{t'}\}_{t' < t+k}; \boldsymbol{\theta}) + \\ &\quad \mathbf{B}_a \boldsymbol{\theta}_{a, T+w} + \mathbf{r}_{t+w} \\ &\quad \vdots \\ \boldsymbol{\mu}_T &= \boldsymbol{\mu}_{T-1} + g(\{\boldsymbol{\mu}_{t'}\}_{t' < T}; \boldsymbol{\theta}) + \mathbf{B}_a \boldsymbol{\theta}_{a, T} + \mathbf{r}_T. \end{aligned} \quad (12)$$

To minimize the regularized loss function in (11), we propose to first plug in all the  $\mu_t$  into the definition of the  $\boldsymbol{\mu}_{t+1}$  for  $t = T, \dots, T+w$  as a function  $\boldsymbol{\mu}_t = \boldsymbol{\mu}_{t-1} + g(\{\boldsymbol{\mu}_{t'}\}_{t' < t}; \boldsymbol{\theta}) + \mathbf{B}_a \boldsymbol{\theta}_{a,t} + \mathbf{r}_t = \dots = \boldsymbol{\mu}_t(\{\boldsymbol{\theta}_{a,t'}\}_{t' < t})$ . Finally, we define the windowed loss function as  $l_{T \rightarrow T+w}(\{\boldsymbol{\theta}_{a,t}\})$  in (13).

$$l_{T \rightarrow T+w}(\{\boldsymbol{\theta}_{a,t}\}) = \sum_{t=T}^{T+w} \|\mathbf{y}_t - \boldsymbol{\mu}_t(\{\boldsymbol{\theta}_{a,t'}\}_{t' < t})\|^2 \quad (13)$$

Finally, by plugging in the windowed loss function in (11), we have (14).

$$\min_{\boldsymbol{\theta}_{a,t}, t \in [T, T+w]} l_{T \rightarrow T+w}(\{\boldsymbol{\theta}_{a,t}\}) + \gamma \sum_{t=T}^{T+w} \|\boldsymbol{\theta}_{a,t}\|_1. \quad (14)$$

Finally, the loss function in (14) can be decomposed into two terms, where  $l_{T \rightarrow T+w}(\{\boldsymbol{\theta}_{a,t}\})$  is differentiable and  $\sum_{t=T}^{T+w} \|\boldsymbol{\theta}_{a,t}\|_1$  is non-differentiable but has a rather simple proximal operator. Therefore, the proximal gradient algorithm can be used to optimize  $\boldsymbol{\theta}_{a,t}$ .



**Proposition 2.** In  $k^{\text{th}}$  iteration,  $\boldsymbol{\theta}_{a,t}^{(k+1)}$  in (14) can be optimized by

$$\boldsymbol{\theta}_{a,t}^{(k+1)} = S_{\gamma/2}(\boldsymbol{\theta}_{a,t}^{(k)} - c \frac{\partial}{\partial \boldsymbol{\theta}_{a,t}} l_{T \rightarrow T+w}(\{\boldsymbol{\theta}_{a,t}\})), \quad (15)$$

where  $c$  is the step size of the proximal gradient algorithm and  $S_{\gamma/2}(\cdot)$  is the soft-thresholding operator.

The proof is given in Supplementary Material.

It is worth noting that for convex and Lipschitz continuous function  $l_{T \rightarrow T+w}(\cdot)$ ,  $\boldsymbol{\theta}_{a,t}$  will converge to the global optimum. However, since  $l_{T \rightarrow T+w}(\cdot)$  is highly non-convex from the deep learning architectures, it is often impossible to guarantee the convergence. However, in reality, we find out with only a few iterations, the algorithm can already obtain a great estimation of the anomaly  $\boldsymbol{\theta}_{a,t}$ . Finally, this estimated  $\boldsymbol{\theta}_{a,t}$  will be used to construct the monitoring statistics, which will be discussed in Section 4.6.

## 4.6 Anomaly Detection Through the Likelihood Ratio Test

After  $\boldsymbol{\theta}_{a,t}$  has been solved, we will construct a likelihood ratio test to detect the change over time. We know from (4) that  $\mathbf{r}_t = \mathbf{y}_t - \boldsymbol{\mu}_{t-1} - g(\{\mathbf{y}_i\}_{i < t}; \boldsymbol{\theta}) = \mathbf{B}_a \boldsymbol{\theta}_{a,t} + \mathbf{e}_t$ . If  $\boldsymbol{\theta}_{a,t} = 0$ , there will be no anomaly and  $\mathbf{r}_t \sim N(0, \sigma^2 I)$ . If there is an anomaly,  $\mathbf{r}_t \sim N(\mathbf{B}_a \hat{\boldsymbol{\theta}}_{a,t}, \sigma^2 I)$ . Therefore, we can propose a likelihood ratio procedure to test the mean of  $\mathbf{r}_t$ , denoted as  $\boldsymbol{\mu}_{\mathbf{r}_t}$  as follows:

$$H_0 : \boldsymbol{\mu}_{\mathbf{r}_t} = 0, \quad H_1 : \boldsymbol{\mu}_{\mathbf{r}_t} = \mathbf{B}_a \hat{\boldsymbol{\theta}}_{a,t}.$$

Moreover, in this paper, we propose to use a likelihood ratio test procedure to test whether there is a change in the estimated anomaly solved by the inverse problem. Finally, according to [42, 43], we can derive the following likelihood ratio-test statistics

$$T_t = 2\hat{\boldsymbol{\theta}}_{a,t}^T \mathbf{B}_a^T (\mathbf{y}_{t+1} - \boldsymbol{\mu}_t - g(\{\mathbf{y}_i\}_{i \leq t}; \boldsymbol{\theta})) - \hat{\boldsymbol{\theta}}_{a,t}^T \mathbf{B}_a^T \mathbf{B}_a \hat{\boldsymbol{\theta}}_{a,t}. \quad (16)$$

Correspondingly, we chose a control limit  $L > 0$  for (16) and define if  $T_t > L$ , the monitoring scheme triggers an OC alarm at time  $t$ .

## 4.7 Tuning Parameter Selection

In this subsection, we will discuss the procedure of selecting the best tuning parameters, including the buffer window size  $w$ , anomaly basis  $\mathbf{B}_a$ , control limit  $L$ , smoothing parameter  $\lambda$ , and sparsity parameter  $\gamma$ .

First, we would like to discuss the procedure of choosing the buffer window size  $w$ . In reality, the best  $w$

depends on the signal-noise ratio, defined by the magnitude of the change divided by the noise magnitude. For a larger signal-noise ratio, it is often easier to detect and a smaller  $w$  is recommended (i.e.,  $w = 0$ ). However, for a smaller signal-noise ratio, it is often recommended to use a larger  $w$ . In reality, it is often hard to know the change magnitude beforehand. Therefore, we suggest to choose to construct the control chart with a buffer window from  $w = 0, 1, \dots, W$ , and select the one with the smallest detection delay. For example, at time  $t$ , we can decide whether time  $t - W$  to  $t$  has an anomaly due to the use of different buffer windows. The algorithm will stop until it triggered the first anomaly.

Second, selecting the anomaly basis is also essential. Selecting a basis for anomalous regions depends on the type of anomalies we aim to detect. For example, if anomalies are randomly scattered over the mean, it is recommended to use an identity basis, i.e.,  $\mathbf{B}_a = I$ . If anomalies form clustered regions, a spline basis or kernel basis can be used. More details about the spatial basis selection of the functional mean and anomalies are given in [44].

Third, we like to discuss the procedure of choosing the control limit  $L$ . Specifically, given a pre-specified IC average run length ( $ARL_0$ ), we propose to select the control limit  $L$  by simulation. Given the complicated spatial-temporal distribution of the data, it is often hard to get the exact distribution of  $T_t$ . In particular, we first choose an initial value for  $L$ , and then compute the  $ARL_0$  of the monitoring statistic in (16) based on a large number of simulation replications, where the IC samples are generated from the IC distribution of the process. If the computed  $ARL_0$  is smaller than the nominal one, we increase the value of  $L$ . Otherwise, we decrease it. We repeat this process until the  $ARL_0$  is achieved with the desired precision. In particular, in the searching procedure, we may use some numerical searching algorithms, such as the bisection search algorithm [45].

Forth, we like to discuss the procedure of choosing the smoothing parameter  $\lambda$ . Here,  $\lambda$  is selected by the cross-validation procedure, where the validation points are randomly selected points across the entire sequence  $\mathbf{y}_t$ . The data at the validation points will be set to 0. The algorithm will try to recover the spatio-temporal mean trend on the validation set and compared it with the original  $\mathbf{y}_t$ .

Finally, we like to discuss the procedure of choosing the sparsity parameter  $\gamma$ . In this procedure,  $\gamma$  will be selected based on the fixed false discovery rate as 5% in the Phase-I analysis with the same basis  $\mathbf{B}_a$  used in Phase-II analysis. We will select  $\gamma$  such as 5% of the  $\theta_{a,t}$  will be detected as an anomaly. The procedure is described in detail in [46].

## 5 Simulation Study

In this section, we will first discuss the data generation and Experimentation Details in Section 5.1 and Section 5.2. The proposed method will be evaluated in terms of metamodeling and mean-trend prediction in Section 5.3.1 and anomaly detection in Section 5.3.2.

### 5.1 Data Generation

We will use the CRN model described in (1) to perform simulations on a one-dimensional cell array (i.e., 1-D cable) with 1500 cells and assume the mono-domain tissue model. Samples (i.e., cell transmembrane potentials) generated by simulations are used to train the metamodel for the spatio-temporal mean trend in the proposed DSTSD model. In this study, we are going to consider two simulation protocols as follows.

- *Case 1:* One stimulation at a variable cycle length of 200ms (5Hz) to 1000ms (1Hz) in a 100ms increment is given to the left end of the cell array, which triggers electrical waves to propagate to the other end of the cable. In addition, more experiments were done by moving the stimulation to the right of the cable in a step of 100 cells. For example, stimulation is given at the left end of the cell array every 300ms. (See Fig. 1a).
- *Case 2:* Two periodic stimulations at a variable cycle length of 200ms (5Hz) to 1000ms (1Hz) in a 100ms increment are given at different locations. The two stimulations are at a variable distance of 300 cells and 600 cells. For example, the stimulations are given at the 1<sup>st</sup> cell and the 600<sup>th</sup> cells (see Fig. 8a and Fig. 9a).

In the Phase-II analysis, we still use the two simulation protocols, Case 1 and Case 2, as described before. We further generate anomalies on top of the regular stimulation  $\mathbf{r}_t$ , which represents cell malfunctioning. The abnormal stimulation is randomly picked along the cell array with an intensity of  $\delta$ . We design the anomaly as a sequence of abnormal points, which will cause a continuous stimulation on the cell. More specifically, we illustrate two cases here with three consecutive abnormal points, causing stimulation at with the amplitude ranging from 4.5 to 11 that will last for 2 ms. In another word, we choose the anomaly  $\mathbf{a}_{s,t} = \delta R_0 1(s \in S_A) 1(t \in S_T)$  in (1), where  $R_0$  is the magnitude of regular stimulation.  $S_A$  is the set of anomalous pixels, and  $S_T$  is the set of time points with anomalies generated.  $\delta$  characterizes the relative intensity difference between anomalies and the spatio-temporal mean trend.  $1(\cdot)$  is the indicator function. In this study, we choose  $S_A = \{s_0, s_0 + 1, s_0 + 2\}$  and  $S_T = \{t_0, t_0 + 1\}$ . Here, the  $s_0$  and  $t_0$  are chosen randomly.  $t_0$  is the start time of the change. A sample of the simulated spatio-temporal mean trend and multiple randomly chosen anomalies are shown in Fig. 1a. In the Phase-I analysis for the training of the

spatio-temporal metamodel, we have generated 15 samples according to Case 1 and 10 samples according to Case 2. Each sample contains 1000 measurements in 1-ms time step.

## 5.2 Experimentation Details

This subsection will give more details on the experimental details in both Phase-I and Phase-II analysis.

In the phase I analysis, we first need to fit the cardiac dynamics with the proposed Conv-LSTM and Conv-WaveNet, which is important to achieve good performance on long-term prediction and anomaly detection. Please see the supplementary material for all the details of the training of Conv-LSTM and Conv-WaveNet.

In the phase-II analysis, a multi-step loss is considered for solving the inverse problem. The window size is set to 3 regarding the trade-off between detection delay and detection accuracy. The learning rate  $c = 0.01$ , and each solving process includes 5 epochs.

## 5.3 Result Comparison

In this subsection, we aim to evaluate the performance of the proposed method in two different parts. First, we will evaluate the performance of the proposed algorithm in terms of predicting the spatio-temporal mean trend in Section 5.3.1. This also evaluates the performance of the proposed DSTSD in terms of metamodeling. 2) Evaluate how well the proposed DSTSD achieves anomaly detection and localization in Section 5.3.2.

### 5.3.1 Spatio-temporal Mean Trend Prediction Accuracy

We compared the prediction accuracy of the learned spatio-temporal metamodel in terms of the spatio-temporal mean trend prediction, i.e.,  $\mu(s, t)$ . relative Mean square error (rMSE) of the predicted mean for the prediction horizon  $\Delta t$  ms were computed as

$$\text{rMSE}(\Delta t) = \frac{1}{NTn_x} \sum_{i,t} \frac{\|\hat{\boldsymbol{\mu}}_{i,t_0}(t_0 + \Delta t) - \boldsymbol{\mu}_{i,t_0}(t_0 + \Delta t)\|^2}{\|\boldsymbol{\mu}_i(t_0)\|^2}, \quad (17)$$

where  $T$  is the length of the sequence in the testing data,  $N$  is the number of testing samples, and  $n_x$  is the length of the spatial dimensions. For the benchmark method, we will compare with the ST-SSD method [8] in terms of future prediction accuracy.

The prediction accuracy of the proposed DSTSD methods based on Conv-WaveNet and Conv-LSTM architectures are calculated and compared using testing data from both cases. For case 1, stimulation at every 800ms is given to the 0th cell of the cable, which generates a series of electrical waves propagating to both ends of the cable. For case 2, a more complicated scenario is considered, where two stimulations

are given at the 1<sup>th</sup> cell and the 600<sup>th</sup> cell every 300ms. Two electrical waves are generated and propagate toward each other and to both ends of the cable. For case 2, given the 2nd stimulation is still inside the cardiac refractory period, it will generate the wave. We will like to evaluate how the proposed model is able to predict cardiac refractoriness behavior. For the benchmark method, we will choose a time-series analysis but treat each spatial dimension independently. The result of the rMSEs of  $\Delta t = 10\text{ms}$ ,  $100\text{ms}$ , and  $200\text{ms}$  are shown in Table 1.

Table 1: Long-term mean trend prediction accuracy MSE for different prediction horizon  $\Delta t = 10, 100, 200$ .

Case 1			
Method	$\Delta t = 10$	$\Delta t = 100$	$\Delta t = 200$
Conv-WaveNet	<b>2.5e-5 (1e-5)</b>	<b>9.9e-4 (3e-4)</b>	<b>2.0e-3 (8e-4)</b>
Conv-LSTM	1.2e-3 (1e-4)	5e-3 (1e-3)	6e-3 (8e-4)
AutoRegressvie	1.6e-2 (3e-4)	1.9e-1 (6e-3)	4.2e-1 (1e-2)
Case 2			
Method	$\Delta t = 10$	$\Delta t = 50$	$\Delta t = 100$
Conv-WaveNet	<b>8.5e-3 (2e-2)</b>	8.5e-2 (8e-3)	2.0e-1 (2e-1)
Conv-LSTM	1.2e-2 (1.8e-2)	<b>1.3e-2 (8e-3)</b>	<b>4.9e-2 (6e-2)</b>
AutoRegressvie	2.7e-2 (2e-2)	3.1e-1 (1e-1)	6.3e-1 (3e-1)

From Table 1, we can conclude that in relatively simple case (i.e., Case 1), Conv-WaveNet out-performs Conv-LSTM. However, for a more complicated case (i.e., Case 2), where two waves merge, and a new excitation is generated within the refractory period, Conv-LSTM is able to predict this refractoriness quite accurately (i.e., a new stimulation is not able to produce any waves.), but Conv-WaveNet failed to predict this effect. For comparison, we also compare with the autoregressive time-series model, which failed to capture any of the trends and result in the largest error. To show this more clearly, we also show the long-term prediction accuracy of both Conv-WaveNet and Conv-LSTM in Fig. 3, which shows the prediction of both Conv-WaveNet and Conv-LSTM compared to the true simulation model. In the supplementary material, we also show the snapshots and the video to demonstrate the performance of the proposed Conv-WaveNet and Conv-LSTM in various scenarios. Overall, we can conclude that Conv-LSTM works better and more robustly given different scenarios compared to Conv-WaveNet, which only works well for relatively simple cases.

Here, we would also like to report the computational time of the proposed metamodells (i.e., Conv-WaveNet and Conv-LSTM) compared to the CRN simulation model to simulate 1s of the cardiac signal. From Table 2, we can conclude that the metamodel is much faster compared to the simulation model (i.e., 0.004s for Conv-LSTM compared to 1.58s for the simulation model) without losing too much accuracy. Conv-LSTM is faster than Conv-WaveNet due to its ability to use the hidden variables to compress the historical observations.

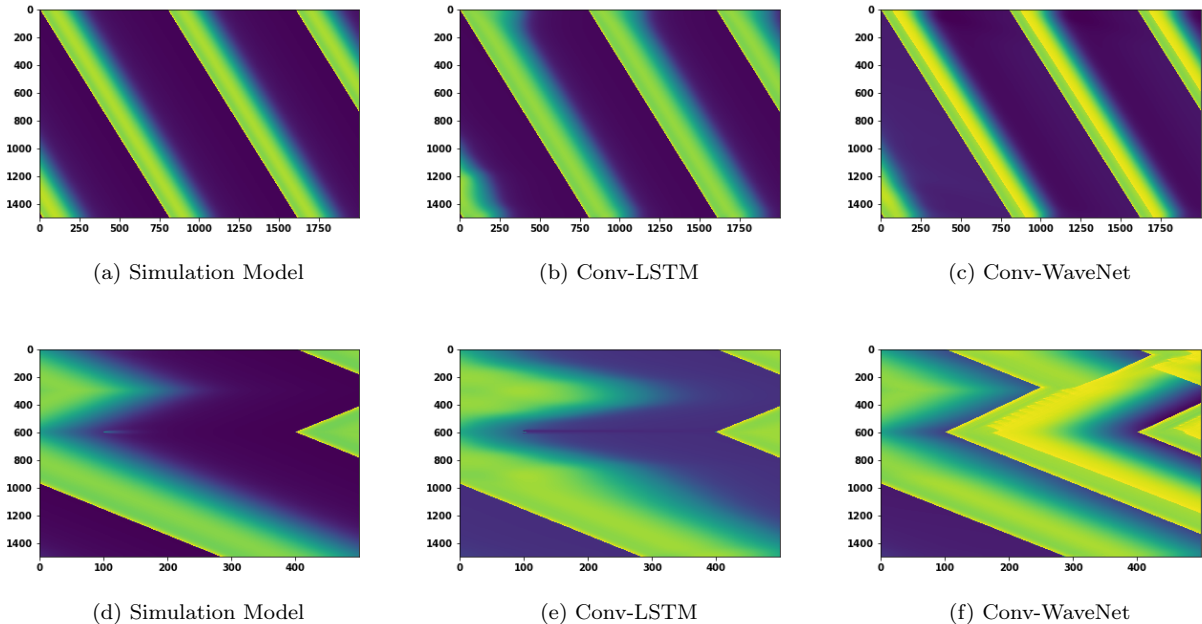


Figure 3: A comparison of Metamodel performance of the proposed Conv-WaveNet and Conv-LSTM. Fig. (a)-(c) illustrated case 1 and (d)-(f) shows case 2. The results show that Conv-WaveNet does not capture the cell refractoriness effect in case 2.

Table 2: The computational time for the original Finite Element Simulation, the proposed Conv-LSMT, and the proposed Conv-WaveNet to simulate 1s of the cardiac signal.

Method	FEM Simulation	Conv-LSTM	Conv-WaveNet
Time	1.58s	0.004s	0.01s

### 5.3.2 Anomaly Detection Accuracy

In this subsection, we will compare the performance of our proposed DSTSD with both architectures from Conv-WaveNet and Conv-LSTM (denoted as 'DSTSD-ConvWaveNet' and 'DSTSD-ConvLSTM') with a few benchmark methods in the literature in terms of anomaly detection. First, we would like to compare with methods that only rely on residual of deep spatio-temporal learning methods. We will use the deep learning architecture with exactly the same architecture, namely the Conv-WaveNet and Conv-LSTM. We also compare with the Hotelling  $T^2$  method as the baseline methods. For Hotelling  $T^2$ , it doesn't have the ability to model the complicated spatio-temporal mean trend, so we use a simple difference along the time dimension to remove the dynamic mean-trend beforehand. We also try the moving average approach and do not find any improvement. Finally, we compared the proposed methods with the ST-SSD methods, which is another spatio-temporal decomposition method but with a fixed smooth spatio-temporal basis [8].

For evaluation, we will compare the performance of the proposed DSTSD with benchmark methods mentioned above in terms of average detection delay and the localization accuracy. (i) To evaluate the

detection delay, we will use the out-of-control Average run length  $ARL_1$ , which is defined as the average detection delay after the change occurs with the fixed in-control  $ARL_0$  as 0. To evaluate the localization accuracy, we will use three additional criteria after a shift is detected: (i) precision, defined as the proportion of detected anomalies that are true anomalies; (ii) recall, defined as the proportion of the anomalies that are correctly identified; (iii) F1-score, a single criterion that combines the precision and recall [47]. It is worth noting that only decomposition-based methods have the ability to isolate the anomaly signals. Therefore, for non-decomposition-based methods such as T2, Conv-LSTM, and Conv-WaveNet, we select a threshold based on Otsu’s method on the residual for source identification [48]. Finally, the average values of these criteria and their standard deviation over 100 simulation replications for  $\delta = 0.2$  and  $\delta = 0.3$  are given in Table 3.

Table 3: The anomaly detection means and standard deviations (including precision, recall, F-1 score, and ARL) for different change magnitudes  $\delta = 0.2$  and  $\delta = 0.3$  for different anomaly detection methods.

$\delta = 0.3$				
Method	precision	recall	F1-score	ARL
T2	0.188(0.087)	0.104(0.049)	0.131(0.061)	53.67(3.08)
Conv-LSTM	0.758(0.041)	0.677(0.034)	0.711(0.033)	24.16(2.67)
Conv-WaveNet	0.354(0.061)	0.250(0.046)	0.292(0.051)	45.35(4.62)
DSTSD-Conv-WaveNet	0.812(0.087)	0.625(0.077)	0.700(0.079)	29.75(4.34)
<b>DSTSD-ConvLSTM</b>	<b>1.000(0.000)</b>	<b>1.000(0.000)</b>	<b>1.000(0.000)</b>	<b>3.20(0.03)</b>
ST-SSD	0.06(0.007)	0.5(0.007)	0.1(0.012)	50.17(5.25)
$\delta = 0.2$				
T2	0.031(0.030)	0.021(0.020)	0.025(0.024)	49.21(1.59)
Conv-LSTM	0.448(0.087)	0.333(0.064)	0.373(0.071)	46.97(5.99)
Conv-WaveNet	0.250(0.625)	0.167(0.041)	0.200(0.050)	53.58(4.14)
DSTSD-ConvWaveNet	0.417(0.075)	0.292(0.050)	0.342(0.059)	42.06(4.47)
<b>DSTSD-ConvLSTM</b>	<b>0.521(0.052)</b>	<b>0.469(0.057)</b>	<b>0.490(0.054)</b>	<b>27.05(4.39)</b>
ST-SSD	0.008(0.001)	0.16(0.025)	0.10(0.012)	50.17(5.25)

From Table 3, we can conclude that the proposed DSTSD-ConvLSTM method achieves the best performance with the smallest detection delay  $ARL_1$ . For example, when  $\delta = 0.3$ , the  $ARL_1 = 0.2$  for the proposed DSTSD-ConvLSTM and the second-best Conv-LSTM has  $ARL_1 = 24.16$ . Similarly, the proposed DSTSD-ConvLSTM has also the best performance for localizing the source. For example, the  $F = 0.521$  for the proposed DSTSD-ConvLSTM  $\delta = 0.2$  and the second-best Conv-LSTM has  $F = 0.448$ . In general, the proposed DSTSD methods are better than the prediction- based model considering both F1 and ARL. T2 doesn’t work well due to its inability to capture the complex spatial-temporal dynamics. ST-SSD failed to detect the anomalies due to its strong smoothness assumption, which is violated by the data generated from the CRN models.

The advantage of the performance is due to the following two reasons: 1) The ability to accurately capture the complex spatio-temporal patterns of the mean trend. The importance of capturing spatio-temporal patterns is demonstrated by comparing the Conv-LSTM, Conv-WaveNet, and the ST-SSD. Conv-LSTM uses the combination of RNN and CNN, which gives the best overall estimation of the spatio-temporal mean trend, which is also shown in Table 1. Conv-WaveNet considers complicated spatial structures. However, due to its use of the auto-regressive model for the temporal structure, it works not as well as Conv-LSTM. ST-SSD relies on the smoothness assumption with a fixed basis in both the spatial dimension and the temporal dimension, which limits its ability to capture and predict complex spatio-temporal dynamics. 2) The ability to separate the anomaly signals considering the sparse structure in the proposed DSTSD framework. In the proposed DSTSD methods (i.e., both DSTSD-ConvLSTM and DSTSD-ConvWaveNet), we solve the inverse problem using the buffered window approach, which achieves a better estimation of the anomaly and leads to smaller  $ARL_1$ .

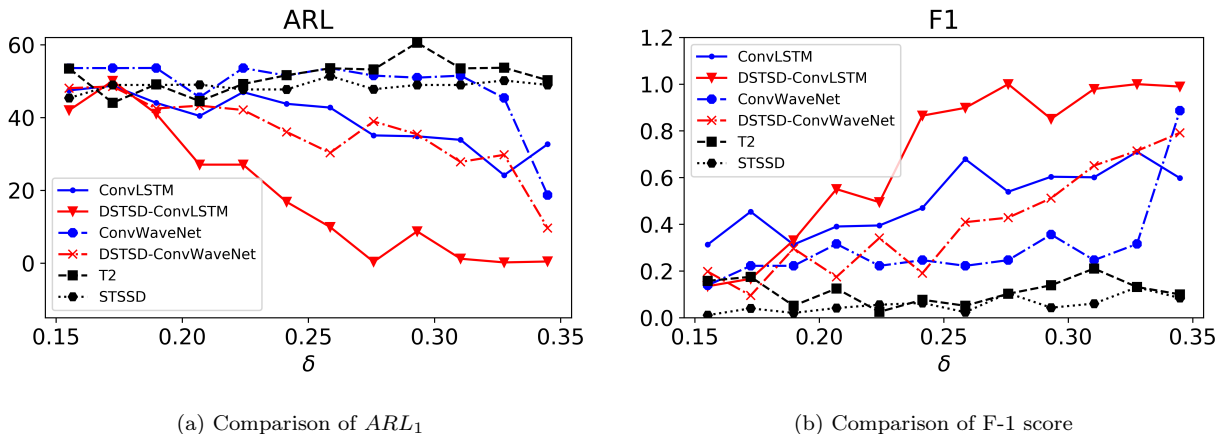


Figure 4: Evaluation criterion for proposed methods. Fig. (a) and (b) shows the Out-of-control Average Run Length (ARL) and the F-1 score of all methods according to different change magnitude  $\delta$ .

We also perform a sensitivity analysis by comparing the proposed algorithm with the benchmark on different change magnitudes  $\delta$ . Here, we have generated abnormal cases with stimulation amplitude ranging from 4.5 to 11 in 0.5 increments, which corresponds to the relative magnitude  $\delta$  from 0.15 to 0.35 in 0.015 increase given the noise level is  $\sigma = 1.5$ . For each case, we generate 16 replications for each delta. We further evaluate the  $ARL_1$  and F1-score for different benchmark methods under these magnitudes (i.e., different  $\delta$ ). It is clear that through solving the inverse problem, two DSTSD-based approaches (i.e., Shown in red) get much better results than their corresponding residual-based methods (i.e., shown in blue). Fig. 4 shows that DSTSD-ConvLSTM can detect the change right away at  $\delta = 0.275$ , while the other methods got a large  $ARL_1$  for every set up we designed. From the result of the F1-score, we can see that DSTSD-ConvLSTM



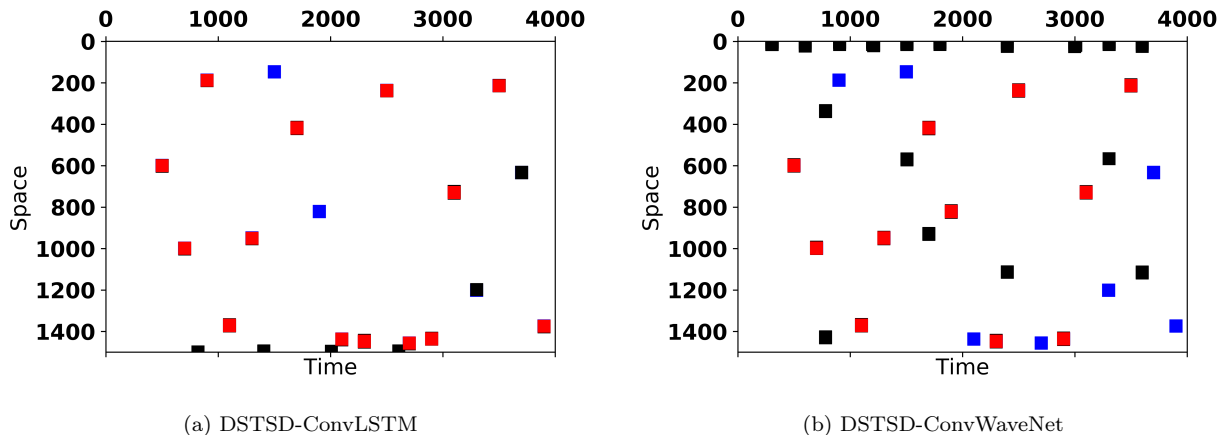


Figure 5: Fig. (a) and (b) show the comparison of the estimated and actual stimulation for the proposed DSTSD-ConvLSTM and DSTSD-ConvWaveNet, respectively. Here, the black square shows the false positives and the blue square shows the false negative. The red square shows the correct predictions.

can identify almost all anomalies as  $\delta$  is close to 0.35 (i.e., F1-score is close to 1).

To show how the proposed algorithm is able to isolate the source location. An example of the detected source for Case I can be seen from Fig. 5. The correctly predicted stimulation points (i.e., true positive) are shown in the red markers, missing stimulation points (i.e., false negative) are shown in blue points, and incorrect predictions (i.e., false positive) are shown in black markers. Through solving the inverse problem, we are able to identify when and where a stimulation happens. For Case I, there is a periodic stimulation at a single location which is cell 1 (can be seen in Fig. 1c and Fig. 1a). From the results, we can see that both methods can identify almost all actual stimulations. In general, DSTSD-ConvLSTM gives a better source localization result with fewer false positives and false negatives compared to DSTSD-ConvWaveNet. In summary, Conv-LSTM performs better than Conv-WaveNet.

## 6 Conclusion

Identifying the cardiac cells that produce electrical impulses in the system governed by complex spatio-temporal dynamics is an important task. In this work, we first proposed a deep spatio-temporal sparse decomposition approach to effectively decompose the original data into a spatio-temporal mean trend as well as the sparse anomaly. To effectively solve the optimization problem, the proximal gradient descent algorithm is applied. To estimate the time and location of the anomaly more accurately, we propose to solve the inverse problem in a window-buffer approach to estimate the anomaly sources accurately. Finally, a sequential likelihood ratio test was proposed to detect the anomaly online. The proposed method is then validated through the data set generated by the CRN model, which is widely used to simulate the changes

of transmembrane potential in human atrial cells. Through extensive comparison, we showed that the proposed methods outperform existing spatio-temporal modeling in terms of the spatio-temporal mean trend prediction (i.e., metamodeling performance), anomaly detection and localization (i.e., anomaly detection performance). For future works, we plan to combine the physical domain knowledge such as the PDEs into the spatio-temporal model for a better generalization power. Furthermore, we are going to extend the current algorithm into multi-dimensional cases, which might be harder due to additional computational challenges.

## A Proof of Proposition 1

*Proof.* Considering the loss function defined in (18).

$$l(\theta, \theta_{a,i,t+1}) = \sum_{i,t} \| e_{i,t+1} - \theta_{a,i,t+1} \|^2 + \lambda \mu'_{t+1} R \mu_{t+1} + \gamma \|\theta_{a,i,t+1}\|_1, \quad (18)$$

where the residual can be defined in (19).

$$e_{i,t+1} = y_{i,t+1} - g(\{y_{i,t'}\}_{t' \leq t}; \theta) - \mu_{i,t} - r_{i,t+1}. \quad (19)$$

Here, the loss function in (18) can be decoupled into each pair of  $(i, t)$  individually. Therefore, each  $\theta_{a,i,t+1}$  can be solved individually by optimizing

$$\hat{\theta}_{a,i,t+1} = \arg \min_{\theta_{a,i,t+1}} \| e_{i,t+1} - \theta_{a,i,t+1} \|^2 + \gamma \|\theta_{a,i,t+1}\|_1 \quad (20)$$

Finally, (20) can be solved by

$$\hat{\theta}_{a,i,t+1} = S_{\gamma/2}(e_{i,t+1}), \quad (21)$$

which is the same as the update step in Proposition 1 given the definition of  $e_{i,t+1}$  in (19).

Finally, we can plug in the solution of  $\hat{\theta}_{a,i,t+1}$  as in (21) into  $l(\theta, \theta_{a,i,t+1})$  defined in (18). We will consider two different cases: □

1. If  $|e_{i,t+1}| > \gamma/2$ ,  $\hat{\theta}_{a,i,t+1} = (|e_{i,t+1}| - \gamma/2) \text{sgn}(e_{i,t+1})$ , therefore, the loss in (21), which is related to

$\theta_{a,i,t+1}$  is

$$\begin{aligned} & \|e_{i,t+1} - \theta_{a,i,t+1}\|^2 + \gamma \|\theta_{a,i,t+1}\|_1 \\ &= \frac{\gamma^2}{4} + \gamma(|e_{i,t+1}| - \gamma/2) \\ &= \gamma|e_{i,t+1}| - \frac{\gamma^2}{4}. \end{aligned}$$

(a) If  $|e_{i,t+1}| < \gamma/2$ ,  $\hat{\theta}_{a,i,t+1} = 0$ ,

$$\begin{aligned} & \|e_{i,t+1} - \theta_{a,i,t+1}\|^2 + \gamma \|\theta_{a,i,t+1}\|_1 \\ &= \|e_{i,t+1}\|^2. \end{aligned}$$

In conclusion, this implies:

$$\|e_{i,t+1} - \theta_{a,i,t+1}\|^2 + \gamma \|\theta_{a,i,t+1}\|_1 = \rho(e_{i,t+1}), \quad (22)$$

$$\text{where } \rho(x) = \begin{cases} x^2 & |x| \leq \frac{\gamma}{2} \\ \gamma|x| - \frac{\gamma^2}{4} & |x| > \frac{\gamma}{2} \end{cases} \text{ is the Huber loss.}$$

*Proof.* By plugging in the definition of (22) into (18), we have  $l_r(\theta) = \sum_i \sum_t (\rho(e_{i,t+1}) + \lambda \mu'_t R \mu_t)$ . By plugging in the definition of  $e_{i,t+1}$ , we can prove proposition 1.  $\square$

## B Proof of Proposition 2

*Proof.* Considering the loss function in

$$\min_{\theta_{a,t}, t \in [T, T+w]} l_{T \rightarrow T+w}(\{\theta_{a,t}\}) + \gamma \sum_{t=T}^{T+w} \|\theta_{a,t}\|_1$$

Since most neural network architecture is Lipschitz continuous [49],  $l_{T \rightarrow T+w}(\{\theta_{a,t}\})$  is Lipschitz continuous. We assume the Lipschitz constance is  $L$ . Therefore, according to the proximal gradient procedure, for each  $\theta_{a,t}$  at each iteration  $k$ , we can minimize the upper bound of  $l_{T \rightarrow T+w}(\{\theta_{a,t}\}) + \gamma \sum_{t=T}^{T+w} \|\theta_{a,t}\|_1$  at iteration

$k$  as

$$\begin{aligned}
\theta_{a,t}^{(k)} &= \arg \min_{\theta_{a,t}} l_{T \rightarrow T+w}(\theta_{a,t}^{(k-1)}) \\
&+ \left\langle \theta_{a,t} - \theta_{a,t}^{(k-1)}, \frac{\partial l_{T \rightarrow T+w}(\{\theta_{a,t}\})}{\partial \theta_{a,t}} \right\rangle \\
&+ \frac{L}{2} \|\theta_{a,t} - \theta_{a,t}^{(k-1)}\|^2 + \gamma \|\theta_{a,t}\|_1
\end{aligned} \tag{23}$$

This can be solved in closed-form as

$$\theta_{a,t} = S_{\gamma/2}(\theta_{a,t}^{(k-1)} - \frac{1}{L} \frac{\partial l_{T \rightarrow T+w}(\{\theta_{a,t}\})}{\partial \theta_{a,t}}).$$

This is the same as the equation in Proposition 2 as the step size  $c = 1/L$ . □

## C Conv-LSTM Architecture

The architectures of Conv-LSTM is shown as follows.

Table 4: Conv-LSTM Architecture

Layer	Conv Kernel Size	Out-channel
Conv1DLSTM+Padding(2)	15	10
Conv1D + ReLU + Padding(2)	3	5
Conv1D	3	1

Here, the notation is introduced as follows:

- Conv1DLSTM to refer to the LSTM with 1-D convolution as defined [40].
- Padding(2): implies the Replication Padding with size 2
- ReLU: Rectified Linear Unit defined as  $\text{relu}(x) = \max(x, 0)$ .

Considering the efficiency of computation, SGD is used as an optimizer for initial steps. During the SGD training process, we select the learning rate as 0.001 and momentum as 0.9. We found after gone through the entire dataset for 10 epoches, the algorithm becomes very unstable. Thus, we switch to AdamW when the fluctuation happens. AdamW is an optimizer improved based on Adam optimizer which have much better generalization behavior. Furthermore, for training the Conv-LSTM, the gradient will be clipped with max norm 0.01 during each iteration avoiding the gradient explosion issue.

## D Conv-Wavenet Architecture

The architectures of Conv-Wavenet is shown as follows.

Table 5: Conv-Wavenet Architecture

Layers	Kernel Size	Dilation size
DilatedConv2D + PReLU+Padding(0,2)	(2, 17)	(1, 1)
DilatedConv2D + PReLU+Padding(0,2)	(2, 17)	(2, 1)
DilatedConv2D + PReLU+Padding(0,2)	(2, 17)	(4, 1)
DilatedConv2D + PReLU+Padding(0,2)	(2, 17)	(8, 1)
DilatedConv2D + PReLU+Padding(0,2)	(2, 17)	(16, 1)
DilatedConv2D + PReLU+Padding(0,2)	(2, 17)	(32, 1)
DilatedConv2D + PReLU+Padding(0,2)	(2, 17)	(64, 1)

Here, the notation is introduced as follows:

- DilatedConv2D: to refer to the 2D dilated convolution and the kernel size is in the format of (Time kernel size, Space kernel size). We will kept the kernel size as (2, 5) and increase the dilation kernel size as  $(2^d, 1)$ , where  $d$  is the dept of the network.
- Padding(0,2): We will use the replication padding as well with time padding size 0 and kernel padding size 2.
- PReLU: Parametric Rectified Linear Unit defined as  $\text{prelu}(x) = \max(x, 0) + a \min(x, 0)$ . where  $a$  is a learnable parameter that control the PReLU layer. When  $a = 0$ , the layer is same as ReLU. When  $a > 0$ , the layer becomes a leaky ReLU layer.

This architecture is inspired by WaveNet [39], which use exponential growth dilation to increase the reception field so that it can model the long-term dependency of the time series data as shown in Figure 6. Here, the major difference with the WaveNet is that we uses the 2D convolution to replace the 1D convolution to model the complex spatial-temporal relationship.

Here, we also apply both SGD and AdamW as the optimizer and switch between two optimizers to ensure stable learning curve. We select same learning rate as 0.001. Beyond that we also apply a Gaussian noise to the original data to make the model more robust against the noise for phase II analysis. From our experience, adding the noise criterion will help the behavior of the model improve a lot.

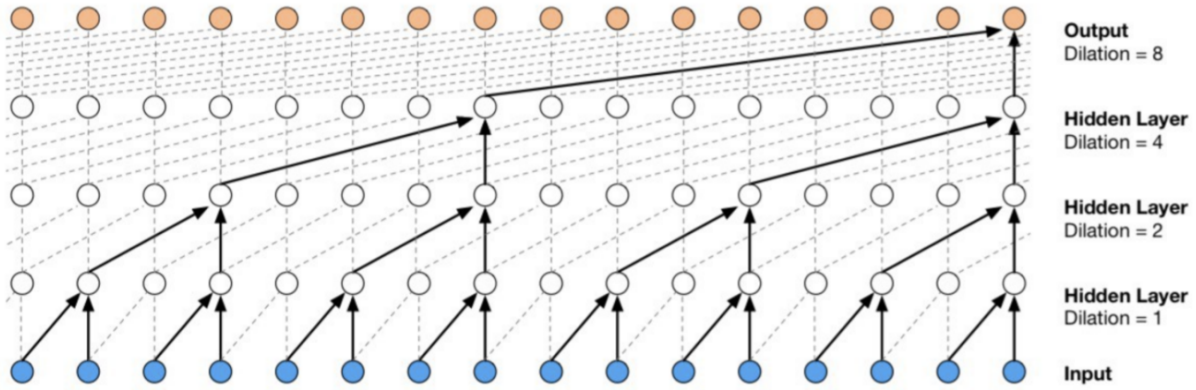


Figure 6: A Demo of WaveNet Architecture [39]

## E Metalearning Performance and Video

We also uploaded the video in the supplementary material on the performance of the metamodels with Conv-LSTM and Conv-WaveNet architectures. There are four videos uploaded, which corresponding to Case 1 and Case 2 with 300ms and 800ms regular stimulation with 550ms-ahead prediction. The snapshots of the videos are shown in Figure 7. In Figure 7 (a) and (c), the stimulation is still within the cell refractory period and should not produce the wave. Only Conv-LSTM is able to capture this trend, where Conv-WaveNet falsely predict the wave is generated.

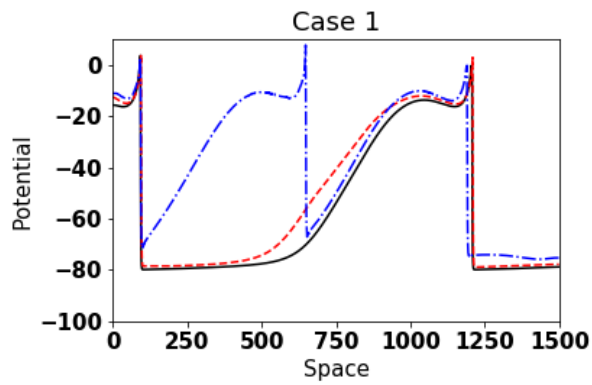
## F Simulation results for FHN model

In this study, we have added another simulation case, where the spatio-temporal dynamics is simulated by Fitz-Hugh-Nagumo model (FHN). The following visualization is actually for the results of FHN model is given here. We also show more intermediate results about signal prediction as shown in Figure.8 and Figure.9 in the following. Table.6 shows the prediction accuracy of the proposed model.

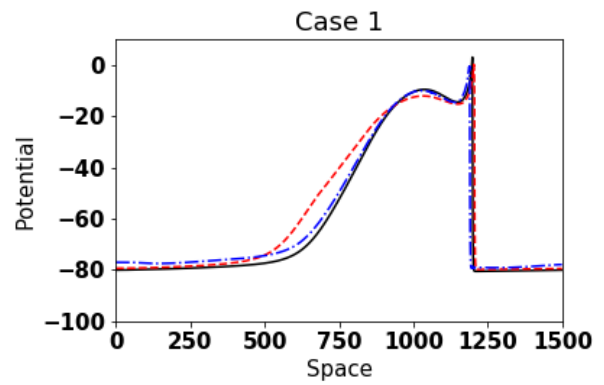
## G Notation Table

## References

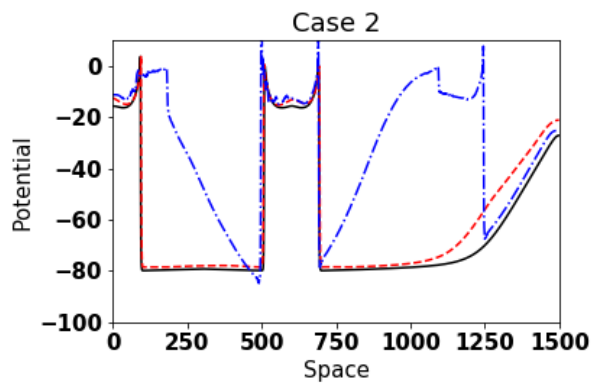
- [1] M. Kropf, D. Hayn, D. Morris, A.-K. Radhakrishnan, E. Belyavskiy, A. Frydas, E. Pieske-Kraigher, B. Pieske, and G. Schreier, "Cardiac anomaly detection based on time and frequency domain features



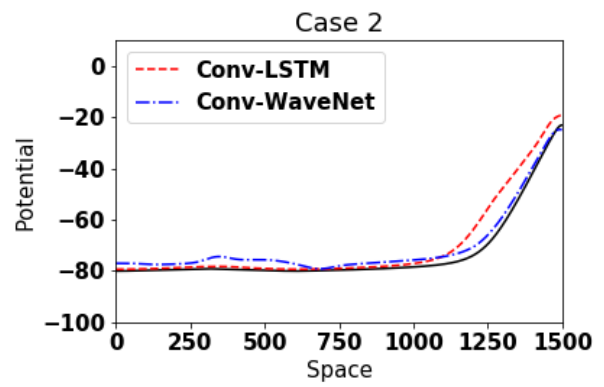
(a) Case 1 with 300ms cycle



(b) Case 1 with 800ms cycle



(c) Case 2 with 300ms cycle



(d) Case 2 with 800ms cycle

Figure 7: 100-time-ahead Prediction for Conv-LSTM and Conv-WaveNet, the full videos are uploaded in the Supplementary Material

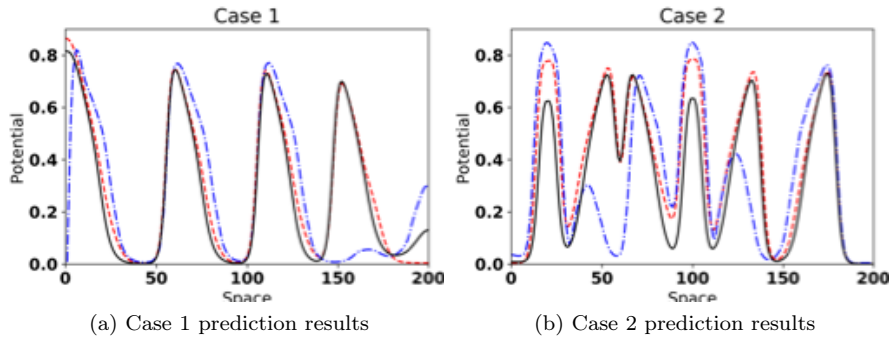


Figure 8: Comparison of the wave pattern at  $\delta t = 200ms$  predicted by AR-CNN and Conv-LSTM vs true data

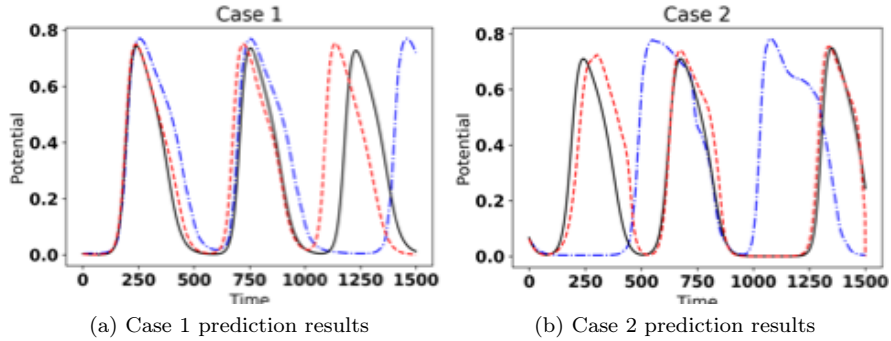


Figure 9: Comparison of the 1500ms-time ahead prediction of AR-CNN, Conv-LSTM, and true data. The origin 0 is the start of prediction time  $t_0$

Table 6: Long-Term prediction accuracy in the noiseless case

Case I			
$\Delta t(ms)$	AR-CNN	Conv-LSTM	AR
5	2.8e-5 (1e-5)	3.9e-5 (1e-5)	2.7e-4 (7e-5)
10	9.0e-5 (3e-5)	4.1e-5 (1e-5)	1.1e-3 (3e-4)
50	1.9e-3 (1e-3)	5.0e-4 (2e-4)	0.023 (0.03)
100	5e-3 (1e-3)	1.0e-3 (6e-4)	0.064 (0.02)
200	1e-2 (4e-3)	4e-3 (6.2e-4)	0.140 (0.04)
Case 2			
delta t	AR-CNN	Conv-LSTM	AR
5	3.8e-5 (2e-5)	3.9e-5 (1e-5)	2.7e-4 (7e-5)
10	8.5e-5 (9e-5)	4.0e-5 (1e-5)	1.1e-3 (3e-4)
50	1.6e-3 (2e-3)	5.0e-4 (2e-3)	0.02 (0.03)
100	5.9e-3 (1e-3)	1.0e-3 (7e-4)	0.06 (0.02)
200	0.013 (8e-3)	1.5e-3 (6e-4)	0.14 (0.04)

using tree-based classifiers,” *Physiological measurement*, vol. 39, no. 11, p. 114001, 2018. 1

[2] A. Presbitero, R. Quax, V. Krzhizhanovskaya, and P. Sloot, “Anomaly detection in clinical data of patients undergoing heart surgery,” *Procedia Computer Science*, vol. 108, pp. 99–108, 2017. 1



- [3] F. Xie, Z. Qu, A. Garfinkel, and J. N. Weiss, “Electrical refractory period restitution and spiral wave reentry in simulated cardiac tissue,” *American Journal of Physiology-Heart and Circulatory Physiology*, vol. 283, no. 1, pp. H448–H460, 2002. 1, 3
- [4] M. Courtemanche, R. J. Ramirez, and S. Nattel, “Tonic mechanisms underlying human atrial action potential properties: insights from a mathematical model,” *American Journal of Physiology-Heart and Circulatory Physiology*, vol. 275, no. 1, pp. H301–H321, 1998. 1, 3, 3
- [5] A. Krizhevsky, I. Sutskever, and G. E. Hinton, “Imagenet classification with deep convolutional neural networks,” in *Advances in neural information processing systems*, Conference Proceedings, pp. 1097–1105. 1
- [6] T. Mikolov, M. Karafiát, L. Burget, J. Černocký, and S. Khudanpur, “Recurrent neural network based language model,” in *Eleventh annual conference of the international speech communication association*, Conference Proceedings. 1
- [7] H. Yan, X. Zhao, Z. Hu, and D. Du, “Physics-based deep spatio-temporal metamodeling for cardiac electrical conduction simulation,” in *2019 IEEE 15th International Conference on Automation Science and Engineering (CASE)*. IEEE, 2019, pp. 152–157. 1
- [8] H. Yan, K. Paynabar, and J. Shi, “Real-time monitoring of high-dimensional functional data streams via spatio-temporal smooth sparse decomposition,” *Technometrics*, vol. 60, no. 2, pp. 181–197, 2018. 1, 2.2, 5.3.1, 5.3.2
- [9] A. Collet, J. Bragard, and P. Dauby, “Temperature, geometry, and bifurcations in the numerical modeling of the cardiac mechano-electric feedback,” *Chaos: An Interdisciplinary Journal of Nonlinear Science*, vol. 27, no. 9, p. 093924, 2017. 2.1
- [10] A. Kaboudian, E. M. Cherry, and F. H. Fenton, “Real-time interactive simulations of large-scale systems on personal computers and cell phones: Toward patient-specific heart modeling and other applications,” *Science advances*, vol. 5, no. 3, p. eaav6019, 2019. 2.1
- [11] S. Dubljevic, S.-F. Lin, and P. D. Christofides, “Studies on feedback control of cardiac alternans,” *Computers & chemical engineering*, vol. 32, no. 9, pp. 2086–2098, 2008. 2.1
- [12] A. Garzón, R. O. Grigoriev, and F. H. Fenton, “Continuous-time control of alternans in long purkinje fibers,” *Chaos: An Interdisciplinary Journal of Nonlinear Science*, vol. 24, no. 3, p. 033124, 2014. 2.1

- [13] C. D. Marcotte and R. O. Grigoriev, “Adjoint eigenfunctions of temporally recurrent single-spiral solutions in a simple model of atrial fibrillation,” *Chaos: An Interdisciplinary Journal of Nonlinear Science*, vol. 26, no. 9, p. 093107, 2016. 2.1
- [14] G. R. Mirams, P. Pathmanathan, R. A. Gray, P. Challenor, and R. H. Clayton, “Uncertainty and variability in computational and mathematical models of cardiac physiology,” *The Journal of physiology*, vol. 594, no. 23, pp. 6833–6847, 2016. 2.1
- [15] E. T. Chang, M. Strong, and R. H. Clayton, “Bayesian sensitivity analysis of a cardiac cell model using a gaussian process emulator,” *PloS one*, vol. 10, no. 6, 2015. 2.1
- [16] R. H. Johnstone, E. T. Chang, R. Bardenet, T. P. De Boer, D. J. Gavaghan, P. Pathmanathan, R. H. Clayton, and G. R. Mirams, “Uncertainty and variability in models of the cardiac action potential: Can we build trustworthy models?” *Journal of molecular and cellular cardiology*, vol. 96, pp. 49–62, 2016. 2.1
- [17] H. Yang, C. Kan, G. Liu, and Y. Chen, “Spatiotemporal differentiation of myocardial infarctions,” *IEEE Transactions on Automation Science and Engineering*, vol. 10, no. 4, pp. 938–947, Oct 2013. [Online]. Available: <http://dx.doi.org/10.1109/tase.2013.2263497> 2.1
- [18] A. Loppini, A. Gizzi, C. Cherubini, E. M. Cherry, F. H. Fenton, and S. Filippi, “Spatiotemporal correlation uncovers characteristic lengths in cardiac tissue,” *Physical Review E*, vol. 100, no. 2, p. 020201, 2019. 2.1
- [19] A. Greisas, Z. Zafrir, and S. Zlochiver, “Detection of abnormal cardiac activity using principal component analysis—a theoretical study,” *IEEE Transactions on Biomedical Engineering*, vol. 62, no. 1, pp. 154–164, 2014. 2.1
- [20] R. Y. Liu, “Control charts for multivariate processes,” *Journal of the American Statistical Association*, vol. 90, no. 432, pp. 1380–1387, 1995. 2.2
- [21] K. Paynabar, C. Zou, and P. Qiu, “A change-point approach for phase-i analysis in multivariate profile monitoring and diagnosis,” *Technometrics*, vol. 58, no. 2, pp. 191–204, 2016. 2.2
- [22] H. Yan, K. Paynabar, and J. Shi, “Image-based process monitoring using low-rank tensor decomposition,” *Automation Science and Engineering, IEEE Transactions on*, vol. 12, no. 1, pp. 216–227, 2015. 2.2
- [23] B. R. Bakshi, “Multiscale pca with application to multivariate statistical process monitoring,” *AICHE journal*, 1998. 2.2

- [24] C. Zhang, H. Yan, S. Lee, and J. Shi, “Dynamic multivariate functional data modeling via sparse subspace learning,” *arXiv preprint arXiv:1804.03797*, 2018. 2.2
- [25] C. Zou, F. Tsung, and Z. Wang, “Monitoring profiles based on nonparametric regression methods,” *Technometrics*, vol. 50, no. 4, pp. 512–526, 2008. 2.2
- [26] P. Qiu, C. Zou, and Z. Wang, “Nonparametric profile monitoring by mixed effects modeling,” *Technometrics*, vol. 52, no. 3, 2010. 2.2
- [27] C. Zou, P. Qiu, and D. Hawkins, “Nonparametric control chart for monitoring profiles using change point formulation and adaptive smoothing,” *Statistica Sinica*, vol. 19, no. 3, p. 1337, 2009. 2.2
- [28] S. I. Chang and S. Yadama, “Statistical process control for monitoring non-linear profiles using wavelet filtering and b-spline approximation,” *International Journal of Production Research*, vol. 48, no. 4, pp. 1049–1068, 2010. 2.2
- [29] K. Paynabar and J. Jin, “Characterization of non-linear profiles variations using mixed-effect models and wavelets,” *IIE Transactions*, vol. 43, no. 4, pp. 275–290, 2011. 2.2
- [30] P. Qiu and D. Xiang, “Univariate dynamic screening system: An approach for identifying individuals with irregular longitudinal behavior,” *Technometrics*, vol. 56, no. 2, pp. 248–260, 2014. 2.2
- [31] D. Xiang, P. Qiu, and X. Pu, “Nonparametric regression analysis of multivariate longitudinal data,” *Statistica Sinica*, vol. 23, pp. 769–789, 2013. 2.2
- [32] K.-W. Cheng, Y.-T. Chen, and W.-H. Fang, “Video anomaly detection and localization using hierarchical feature representation and gaussian process regression,” in *Proceedings of the IEEE Conference on Computer Vision and Pattern Recognition*, 2015, pp. 2909–2917. 2.2
- [33] Y. Zhao, B. Deng, C. Shen, Y. Liu, H. Lu, and X.-S. Hua, “Spatio-temporal autoencoder for video anomaly detection,” in *Proceedings of the 25th ACM international conference on Multimedia*, 2017, pp. 1933–1941. 2.2
- [34] M. Ravanbakhsh, M. Nabi, E. Sangineto, L. Marcenaro, C. Regazzoni, and N. Sebe, “Abnormal event detection in videos using generative adversarial nets,” in *2017 IEEE International Conference on Image Processing (ICIP)*. IEEE, 2017, pp. 1577–1581. 2.2
- [35] M. Mathieu, C. Couprie, and Y. LeCun, “Deep multi-scale video prediction beyond mean square error,” *arXiv preprint arXiv:1511.05440*, 2015. 2.2

- [36] A. Munawar, P. Vinayavekhin, and G. De Magistris, “Spatio-temporal anomaly detection for industrial robots through prediction in unsupervised feature space,” in *2017 IEEE Winter Conference on Applications of Computer Vision (WACV)*. IEEE, 2017, pp. 1017–1025. 2.2
- [37] D. M. Harrild and C. S. Henriquez, “A computer model of normal conduction in the human atria,” *Circulation research*, vol. 87, no. 7, pp. e25–e36, 2000. 3
- [38] S. Zahid, H. Cochet, P. M. Boyle, E. L. Schwarz, K. N. Whyte, E. J. Vigmond, R. Dubois, M. Hocini, M. Haïssaguerre, P. Jaïs *et al.*, “Patient-derived models link re-entrant driver localization in atrial fibrillation to fibrosis spatial pattern,” *Cardiovascular research*, vol. 110, no. 3, pp. 443–454, 2016. 3
- [39] A. v. d. Oord, S. Dieleman, H. Zen, K. Simonyan, O. Vinyals, A. Graves, N. Kalchbrenner, A. Senior, and K. Kavukcuoglu, “Wavenet: A generative model for raw audio,” *arXiv preprint arXiv:1609.03499*, 2016. 4.2.1, D, 6
- [40] T. N. Sainath, O. Vinyals, A. Senior, and H. Sak, “Convolutional, long short-term memory, fully connected deep neural networks,” in *2015 IEEE International Conference on Acoustics, Speech and Signal Processing (ICASSP)*. IEEE, Conference Proceedings, pp. 4580–4584. 4.2.2, C
- [41] A. Račkauskas and C. Suquet, “Hölder norm test statistics for epidemic change,” *Journal of statistical planning and inference*, vol. 126, no. 2, pp. 495–520, 2004. 4.5
- [42] K. Wang and W. Jiang, “High-dimensional process monitoring and fault isolation via variable selection,” *Journal of Quality Technology*, vol. 41, no. 3, pp. 247–258, 2009. 4.6
- [43] C. Zhang, H. Yan, S. Lee, and J. Shi, “Weakly correlated profile monitoring based on sparse multi-channel functional principal component analysis,” *IIE Transactions*, vol. 50, no. 10, pp. 878–891, 2018. 4.6
- [44] H. Yan, K. Paynabar, and J. Shi, “Anomaly detection in images with smooth background via smooth-sparse decomposition,” *Technometrics*, vol. 59, no. 1, pp. 102–114, 2017. 4.7
- [45] P. Qiu, “Distribution-free multivariate process control based on log-linear modeling,” *IIE Transactions*, vol. 40, no. 7, pp. 664–677, 2008. 4.7
- [46] H. Yan, K. Paynabar, and J. Shi, “Akm2d: An adaptive framework for online sensing and anomaly quantification,” *IIE Transactions*, pp. 1–15, 2019. 4.7
- [47] C. Van Rijsbergen, “Information retrieval,” 1979. 5.3.2

- [48] N. Otsu, “A threshold selection method from gray-level histograms,” *Automatica*, vol. 11, no. 285-296, pp. 23–27, 1975. 5.3.2
- [49] A. Virmaux and K. Scaman, “Lipschitz regularity of deep neural networks: analysis and efficient estimation,” in *Advances in Neural Information Processing Systems*, 2018, pp. 3835–3844. B